nature communications

The urotensin II receptor triggers an early meningeal response and a delayed macrophage-dependent vasospasm after subarachnoid hemorrhage in male mice

Martin Pedard[1,2], Lucie Prevost [1,2,9], Camille Carpena[3,9], Brian Holleran[4,9], Laurence Desrues[1,2,9], Martine Dubois[1,2,9], Celeste Nicola[1,2], Roxane Gruel[1,2], David Godefroy[2,5], Thomas Deffieux [6], Mickael Tanter [6], Carine Ali[7], Richard Leduc [4], Laurent Prézeau[3], Pierrick Gandolfo[1,2], Fabrice Morin[1,2], Olivier Wurtz[1,2], Thomas Bonnard [7], Denis Vivien [7,8] & Hélène Castel [1,2] ✉

Subarachnoid hemorrhage (SAH) can be associated with neurological deficits and has profound consequences for mortality and morbidity. Cerebral vasospasm (CVS) and delayed cerebral ischemia affect neurological outcomes in SAH patients, but their mechanisms are not fully understood, and effective treatments are limited. Here, we report that urotensin II receptor UT plays a pivotal role in both early events and delayed mechanisms following SAH in male mice. Few days post-SAH, UT expression is triggered by blood or hemoglobin in the leptomeningeal compartment. UT contributes to perimeningeal glia limitans astrocyte reactivity, microvascular alterations and neuroinflammation independent of CNS-associated macrophages (CAMs). Later, CAM-dependent vascular inflammation and subsequent CVS develop, leading to cognitive dysfunction. In an SAH model using humanized $UT^{h+/h+}$ male mice, we show that post-SAH CVS and behavioral deficits, mediated by UT through $Gq/PLC/Ca^{2+}$ signaling, are prevented by UT antagonists. These results highlight the potential of targeting UT pathways to reduce early meningeal response and delayed cerebral ischemia in SAH patients.

Stroke, comprising ischemic and hemorrhage insults, represents the second leading cause of death worldwide. Subarachnoid hemorrhage (SAH), which often results from a ruptured cerebral aneurysm, involves the leakage of arterial blood into the subarachnoid space, affecting the inner pia mater surface, the arachnoid membrane and villi, cisterns and ventricles[1,2]. The mean age of SAH patients ranges from 50 to 60 years, and there is a notable prevalence of poor outcomes, with a case-fatality rate for SAH of approximately 40% after 1 year[3]. Survivors of SAH commonly endure severe cognitive sequelae including deficits in verbal and nonverbal memory, visual-spatial

[1]Univ Rouen Normandie, Inserm, Normandie Univ, CBG UMR 1245, Rouen, France. [2]Institute of Research and Innovation in Biomedicine (IRIB), Rouen, France. [3]Institut de Génomique Fonctionnelle, Univ. Montpellier, CNRS, Inserm, Montpellier, France. [4]Department of Pharmacology-Physiology, Faculty of Medicine and Health Sciences, Université de Sherbrooke, Sherbrooke, QC, Canada. [5]Univ Rouen Normandie, Inserm, Normandie Univ, NorDiC UMR 1239, Rouen, France. [6]Institute Physics for Medicine, Inserm U1273, CNRS UMR 8631, ESPCI Paris, Paris Sciences et Lettres PSL University, Paris, France. [7]Normandie Université, UNICAEN, INSERM U1237, PhIND "Physiopathology and Imaging of Neurological Disorders", Institut Blood and Brain @ Caen-Normandie, GIP Cyceron, Caen, France. [8]Centre Hospitalier Universitaire Caen, Department of Clinical Research, Caen, France. [9]These authors contributed equally: Lucie Prevost, Camille Carpena, Brian Holleran, Laurence Desrues, Martine Dubois. ✉e-mail: helene.castel@univ-rouen.fr

function, executive function or psychomotor speed and significant asthenia, which impact their daily lives and ability to return to work[4-6].

The key contributors to unfavorable clinical outcomes following SAH include angiographic cerebral vasospasm (CVS) and delayed cerebral ischemia (DCI), this later being primarily considered consecutive to, but now thought to be at least in part independent of, CVS. The standard of care of SAH is the calcium channel blocker nimodipine (Nimotop©), with the goal of preventing arterial spasms and improving cerebral blood flow[7]. However, the modest CVS-independent beneficial effect of nimodipine fuels the current cause-and-effect relationship debate[8,9]. The severity of early bleeding and local brain inflammatory reactions, marked by the presence of infiltrating or resident neutrophils, are also implicated in the poor outcomes of patients following SAH[10-13].

Clinical trials with endothelin-1 (ET-1) receptor (ETA) antagonists likely preventing Gq/Ca^{2+} signaling and vasospasm, statins or intracisternal magnesium sulfate infusion have shown significant improvements in CVS, but morbidity and/or clinical outcomes have remained largely unchanged[14-16]. Cilostazol, a selective phosphodiesterase III inhibitor known for its multifactorial vascular relaxing functions, has shown relative efficacy toward CVS but only a modest reduction in the rate of cerebral ischemia in SAH patients[17]. These findings suggest that targeting vascular dysfunction may only partially prevent CVS-mediated DCI and/or SAH-induced neurological deficits.

To identify early contributors to CVS and DCI, some previous studies focused on brain structures and regions early impacted by SAH. Notably, the first brain region covered by blood components and plasma is the pia matter, the innermost layer of fibroblast-like cells, vessels, and sentinel immune cells of the meninges that contains and is in contact with the cerebrospinal fluid (CSF). The contribution of this meningeal compartment to cross-regulating astrocyte reactivity[18,19] after traumatic CNS injury and its involvement in inflammation leading to hydrocephalus[20] after bleeding are underestimated, highlighting the need for a better understanding of early brain injury (EBI), microcirculatory dysfunction, and the mechanisms leading to vasospasm following SAH.

As vascular smooth muscle cells and endothelial inflammation have been involved in post-SAH CVS, we previously investigated the contribution of the vasoactive peptide urotensin II (UII) to this condition and found a link between elevated UII plasma levels and CVS after SAH in humans[21]. UII which acts on the G protein-coupled receptor (GPCR) has been associated with various pathophysiological conditions, including atherosclerosis, heart failure, hypertension, preeclampsia, diabetes, renal disease, vascular dementia, and postischemic hyperfusion[22,23]. The underlying contribution of UII to all these different conditions involves the UT/Ca^{2+}-induced contraction of vascular smooth muscle, which results in increased vascular tone, increased tissue factor and adhesion molecule expression, the inflammation of vessel walls, and the chemotactic recruitment and polarization of monocytes[24-26]. Interestingly, we previously showed that the UT antagonist/biased ligand urantide prevents both CVS and locomotor deficits in a preclinical mouse model of mild SAH[21]. The lack of the efficacy of current therapy widely based on vascular tone and mainly focusing on CVS requires to understand and target combined multiple brain insults post-SAH.

The aim of the study is to elucidate whether UT and its G protein coupling pathways play a central role in early meningeal cell inflammation, CVS, and consecutive behavioral alterations. Utilizing in vitro and integrated in vivo approaches, we found that UT expression is triggered by the blood- and hemoglobin-induced upregulation of hypoxia-inducible factor-1α (HIF-1α) in the leptomeningeal cell compartment. UT appeared as a crucial regulator of early glia limitans activation in the perimeningeal barrier following SAH, leading to CNS-associated macrophage (CAM)-driven vascular inflammation, CVS, and behavioral alterations. By leveraging a humanized $UT^{h+/h+}$ SAH mouse model and pharmacological drugs targeting Gq signaling, we demonstrated the causal impact of Gq/PLC pathway in the pia and arachnoid membrane layers of the leptomeninges, inducing astrocyte activation of the glia limitans, CVS and alterations in visual exploration and sensorimotor function. We also identified UII-induced UT coupling to G proteins and β-arrestins 1 and 2, while the use of biased ligands and/or antagonists targeting these pathways prevented SAH-induced meningeal reactivity, CVS, and behavioral deficits in $UT^{h+/h+}$ mice. SAH pathophysiology needs immediate medical attention and emergency treatment to reduce the risk for lifelong brain damage. The new understanding of the contribution of UII and UT system in the early meningeal cell responses and delayed events should reduce the gaps in our understanding of SAH and help to evaluate new strategies for stroke patient outcome.

Results

UT is expressed in the leptomeninges and brain vasculature and controls behavioral deficits in SAH

To identify the key early mechanisms potentially responsible for all SAH consequences, we first focused on the initial brain region affected by blood components during SAH – the meningeal compartment. Specifically, we aimed to determine whether UT might be expressed in leptomeningeal cells and activated at onset of the first bleeding event. To address this, SAH was induced in wild-type $UT^{+/+}$ or nonconditional transgenic UT knockout male mice ($UT^{-/-}$ C57Bl/6) by two consecutive injections of arterial blood into the cisterna magna as previously described, and sham animals received artificial cerebral spinal fluid (aCSF, sham)[27,28]. To assess the early stage post-SAH localization of blood deposition, the brains were collected 24 h after SAH (D1) (Fig. 1a). Using 3D images of cleared intact skulls, we demonstrated the presence of erythrocytes (TER-119$^+$) on the surface of the cortex of the brain in contact with the leptomeninges and along cortical penetrating arterioles. Interestingly, TER-119$^+$ staining was also detected in marrow-containing cavities and along some skull channels connecting the meninges to the skull (Fig. 1b). Immunohistochemical experiments using antibodies against mature neurons (anti-NeuN; Supplementary Fig. 1a), astrocytes (anti-GFAP, Supplementary Fig. 1b), or vascular compartment lectin$^+$ cells (pericytes: anti-NG2, Supplementary Fig. 1c; and smooth muscle cells: anti-α-SMA, Supplementary Fig. 1d) revealed the exclusive expression of UT in lectin$^+$ penetrating arterioles and capillaries of SAH model mice who were administered blood.

To assess the late-stage post-SAH localization of blood deposition, brains were analyzed at day seven after SAH (D7). At this timepoint (Fig. 1c), UT expression was markedly increased in the endothelial compartment (CD31$^+$/podocalyxin$^+$) of pial surface vessels, cortical penetrating arterioles SAH $UT^{+/+}$ compared to $UT^{+/+}$ sham mice (Fig. 1d). In sham $UT^{+/+}$ mice and $UT^{-/-}$ mice with UT promoter-induced LacZ expression (Supplementary Fig. 2), weak UT or no β-galactosidase (β-Gal) staining was observed (Fig. 1e). However, after these $UT^{+/+}$ and $UT^{-/-}$ mice were subjected to SAH, UT, and β-Gal were expressed at D7 in different brain areas, such as the leptomeninges, choroid plexus, and hippocampus (Fig. 1e), and importantly in posterior cerebral artery, cortical and hippocampal capillaries and the endothelial basement membranes of the choroid plexus (Fig. 1f). Thus, SAH markedly increases UT expression not only in the cerebral endothelial compartment but also in leptomeningeal fibroblasts acutely exposed to blood.

To investigate whether the de novo expression of UT in these vascular and leptomeningeal compartments is involved in long-term cognitive deficits, we examined spontaneous activity, sensorimotor function, and anxiety/depressive-like behaviors in $UT^{+/+}$ and $UT^{-/-}$ sham and SAH mice using the open field test, beam walking test and the forced-swim and elevated-plus maze tests, respectively, at D6-D7 after surgery (Fig. 2a). Spontaneous activity, evaluated as the distance crossed and the number of leans, was significantly impaired in $UT^{+/+}$

Article
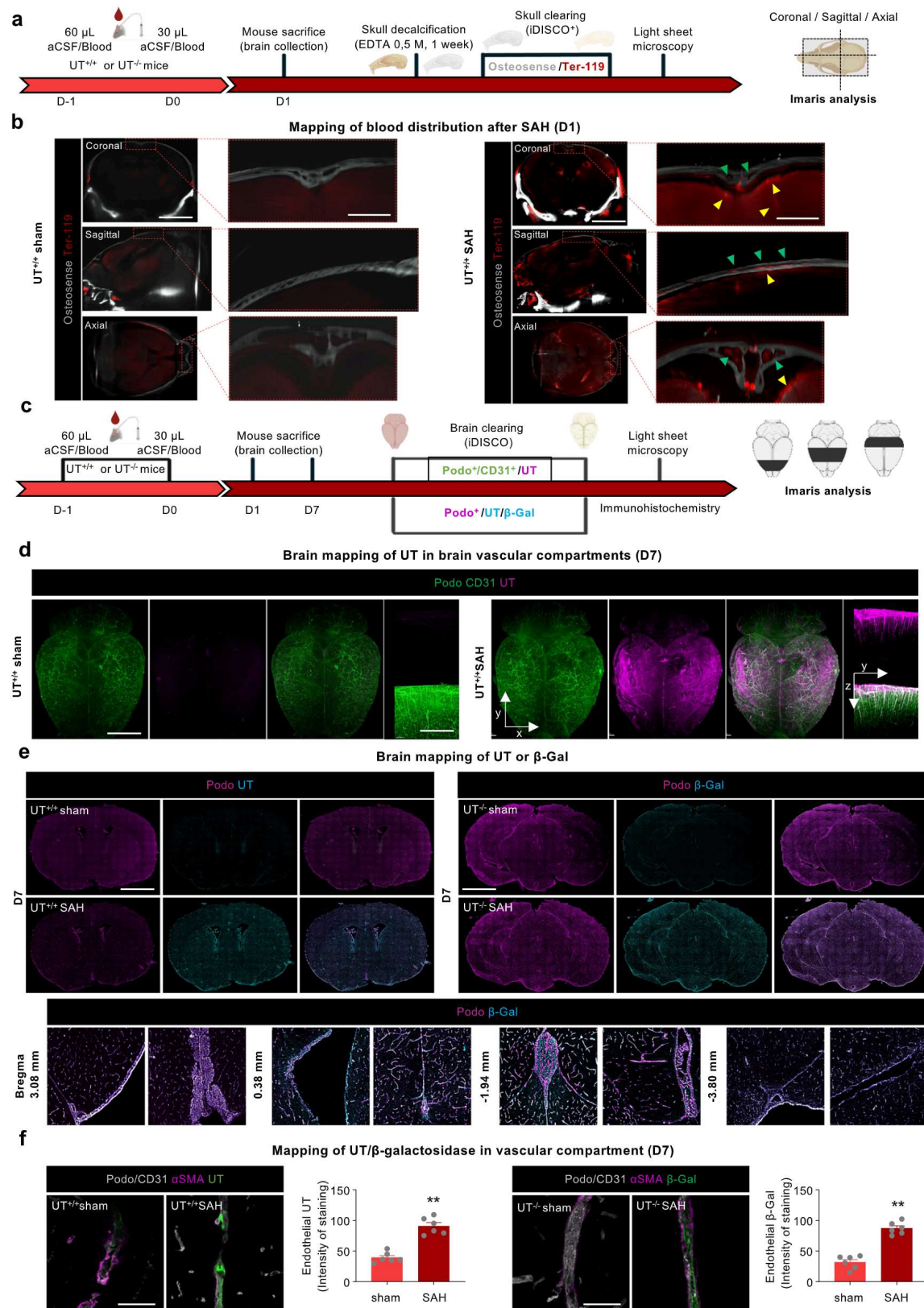
SAH mice compared to UT^{+/+} sham mice, while that of UT^{-/-} sham and SAH mice was unaffected (Fig. 2b). SAH animals showed significantly decreased sensorimotor function (Fig. 2c) and increased depressive (resignation) (Fig. 2d) and anxiety-like behaviors (Fig. 2e) compared to UT^{+/+} sham mice; both groups of UT^{-/-} mice showed no differences with control UT^{+/+} mice. At D14, UT^{+/+} SAH mice showed a significantly

reduced preference index in the novel object recognition test (Fig. 2f) compared with that in the other groups, indicating delayed short-term memory defect post-SAH. To assess spatial learning, long-term memory, and behavioral flexibility, the Morris water maze test was performed at D1-4; UT^{+/+} SAH mice took significantly longer to reach the platform than did UT^{+/+} sham, UT^{-/-} sham, or UT^{-/-} SAH mice (Fig. 2g) for

Article　　　　　　　　　　　　　　　　　　https://doi.org/10.1038/s41467-024-52654-2

Fig. 1 | The urotensinergic system is overexpressed in the cerebral vascular endothelial compartment after SAH. a Timeline of SAH surgery, mouse sacrifice for skull collection and clearing for the iDISCO+ procedure. **b** Example of Ter-119+ (red) erythrocyte distribution around leptomeninges and into the Osteosense+ (gray) skull from a transparent 8-week-old UT+/+ brain 24 hours after surgery (representative of one of the two tested mice/condition). Scale bar = 1 mm. Zoomed scale bar = 200 μm. **c** Timeline of SAH surgery, mouse sacrifice for brain collection, brain IHC and clearing for iDISCO+ procedure, light sheet imaging and Imaris analysis to measure vascular diameter and density. **d** Example of characterization of UT (magenta) from a transparent 8-week-old UT+/+ brain generated by iDISCO+ showing endothelial (Podo+/CD31+ in green) UT overexpression in SAH (blood) compared to sham (aCSF) conditions. Scale bar = 1 mm. Zoomed X-stack generated with Imaris showing at least endothelial UT overexpression in pial and penetrating arterioles under SAH conditions (representative of one of the three tested mouse brains). Scale bar = 200 μm. **e** Mouse brain mapping of immunolabeling of UT

(cyan) or bacterial β-galactosidase (β-Gal, cyan) under the *UTS2R* promoter and of Podo (podocalyxin)+ cerebral endothelium (magenta) in UT+/+ or UT-/- mice from aCSF- and blood-injected mouse brains 7 days (D7) after SAH. Scale bar = 1 mm (representative of one of the two tested mouse brains). Zoomed scale bar = 200 μm. **f** Immunolabeling of UT or β-Gal (green) in the Podo+/CD31+ endothelium (white) and α-smooth muscle actin+ (αSMA, magenta) in cortical arterioles from aCSF- and blood-injected UT-/- mice. Quantification of endothelial UT and β-Gal intensities (*n* = 6/condition). Scale bar = 50 μm. UT and β-Gal are observed in the Podo/CD31+ endothelium and not in the αSMA+ layer in arterioles from SAH mice. Values are expressed as the mean ± SEM. **P < 0.01 (non-normally distributed, comparison of two groups, unpaired two-sided Mann–Whitney test). Source data are provided as a Source Data file. **a, c** created with BioRender.com released under a Creative Commons Attribution-NonCommercial-NoDerivs 4.0 International license (https://creativecommons.org/licenses/by-nc-nd/4.0/deed.en).

each day of trial. In addition, analysis of spatial learning strategies and behavioral flexibility from D1 to D4 revealed that UT+/+ SAH mice displayed lower cognitive scores than did UT+/+ sham, UT-/- sham or UT-/- SAH mice (Fig. 2h) but did not show altered learning or long-term memory after the SAH event.

To investigate the neurobiological markers in the hippocampus recognized as being involved in the neural map of space and cognitive functions, we next evaluated hippocampal neurogenesis as a marker of brain vascular injury[29,30]. The number of neurons coimmunolabeled with antibodies directed against the DNA synthesis and cell division marker BrdU and the mature neuronal marker NeuN was significantly reduced in UT+/+ SAH mice compared to UT+/+ sham mice, while no difference was observed between UT-/- sham and SAH mice (Fig. 2i), indicating reduced neurogenesis after bleeding. We also observed significant increases in the area and intensity of GFAP and Iba1 (to label astrocytes and microglia, respectively) staining exclusively in UT+/+ mice at D7 (Fig. 2j). The expression of these astrocytic and microglial neuroinflammatory indicators likely accompanies the delayed behavioral, emotional, and cognitive deficits observed in mice expressing UT subjected to SAH. These results confirm UT as a major contributor to long-term sensorimotor deficits powered by an altered hippocampal neurogenesis and neuroinflammation in a murine model of mild SAH[21].

Delayed CVS depends on UT and requires UII contained in the blood

In order to make a link with clinical studies stating poor neurological outcomes and cognitive deficits[31,32] likely attributed to a secondary ischemic event consecutive to CVS, here were investigated vascular inflammation and microvascular components as well as CVS post-SAH. We thus characterized the cerebral vascularization network by immunohistochemistry with the combination of anti-CD31 and anti-Podocalyxin antibodies in iDISCO-cleared brains. This SAH-induced UT was associated with significant decreases in both mean vessel diameter and density in the occipital, parietal, and frontal lobes after SAH in UT+/+ mice compared to sham mice (Fig. 3a and Supplementary Fig. 3a). Interestingly, similar vascular networks were observed in UT-/- SAH and UT+/+ sham mice (Fig. 3a). To investigate the contribution of UT to CVS, we measured the lumen area/wall thickness ratio of podocalyxin+/αSMA+ vessels to provide a quantitative measure of CVS in rodents. In UT+/+ mice, a progressive reduction in the lumen area/wall thickness ratio in the middle cerebral artery (MCA), anterior cerebral artery (ACA) and basilar artery (BA) (Supplementary Fig. 3b), concomitant with the enhanced endothelial expression of UT in podocalyxin+ endothelial cells of the MCA (Fig. 3b), was observed under SAH conditions from D1 to D7. Moreover, in UT+/+ mice, UT expression and CVS magnitude were strongly correlated (Fig. 3b, rs = -0.746, p = 0.0000002), while no CVS was detected in

the podocalyxin+/CD31+/α-SMA+/β-Gal+ MCAs of UT-/- SAH mice (Fig. 3b and Supplementary Fig. 3).

To investigate the binding of UII to UT, Qdot655 coupled to biotinylated UII (QD655-UII) (10^{-5} M) was intravenously administered to UT+/+ or UT-/- mice at D7 (Supplementary Fig. 4a). Increased QD655-UII fluorescence was observed along lectin+ pial surface vessels and capillaries and/or venules of UT+/+ SAH mice (Supplementary Fig. 4b). Additionally, QD655-UII particles were specifically retained in the spasmed MCA endothelium at D7 (Supplementary Fig. 4c). We hypothesized that SAH leads to the diffusion of blood containing UII within the subarachnoid space and perivascular area, activating UT overexpressed by vessels and the leptomeningeal compartment. In line with our hypothesis, UII was detected near TER-119+ erythrocytes in UT+/+ SAH mice (Fig. 3c) while the co-occurrence of these labelings is positively correlated (rs = −0.918, p = 0.0000002). This proximal distribution was observed in AKAP12+ leptomeningeal fibroblasts in both UT+/+ and UT-/- SAH mice (Fig. 3c). This finding was confirmed at D1 and D7 in UT+/+ and UT-/- SAH mouse brains through immunostaining for another meningeal fibroblast marker, ERTR7 (Supplementary Fig. 5a). Subsequent analysis revealed that UII levels were unchanged in the MCA endothelial layer (Supplementary Fig. 5b). Together, these data reveal a contribution of UII-containing blood/plasma covering the meningeal layers just after bleeding and particularly the leptomeninges in which UT expresses in SAH conditions.

UT expression drives brain vascular inflammation and reduces blood flow following SAH

Primary factors contributing to CVS are endothelial activation evidenced by the endothelial expression of luminal VCAM-1[33]. Using immunohistochemistry, we observed increased endothelial VCAM-1 expression in the brains of UT+/+ SAH mice, concomitant with positive UT labeling in cortical capillaries of the MCA territory from D1 to D7 (Supplementary Fig. 6). This phenomenon was also observed in vivo using high-resolution magnetic resonance (MR)-based molecular imaging of MPIO-VCAM-1 as previously validated[34] (Fig. 4a, b). Compared to UT+/+ sham mice, a marked increase in the MR void signal, induced by the binding of MPIO-VCAM-1 to VCAM-1-positive vessels, was observed in various brain regions from the pons to the frontal cortex in UT+/+ SAH mice (Fig. 4c). Of note, MR void signal was found similar between UT-/- sham and SAH mice, and UT+/+ sham mice (Fig. 4c).

Edema is detectable several hours post-SAH[35,36] due to a transient increase in intracranial pressure and cerebral hypoperfusion[37], both of which precede vascular inflammation[38] and autoregulatory dysfunction[39]. Using in vivo T2-weighted MRI, we found edema primarily in the periventricular white matter of UT+/+ but not UT-/- SAH mice at D2 and up to D7 postinjury (Fig. 4d). In UT+/+ SAH mice, ventricular enlargement positively correlated with the MPIO-VCAM-1 MR

Article
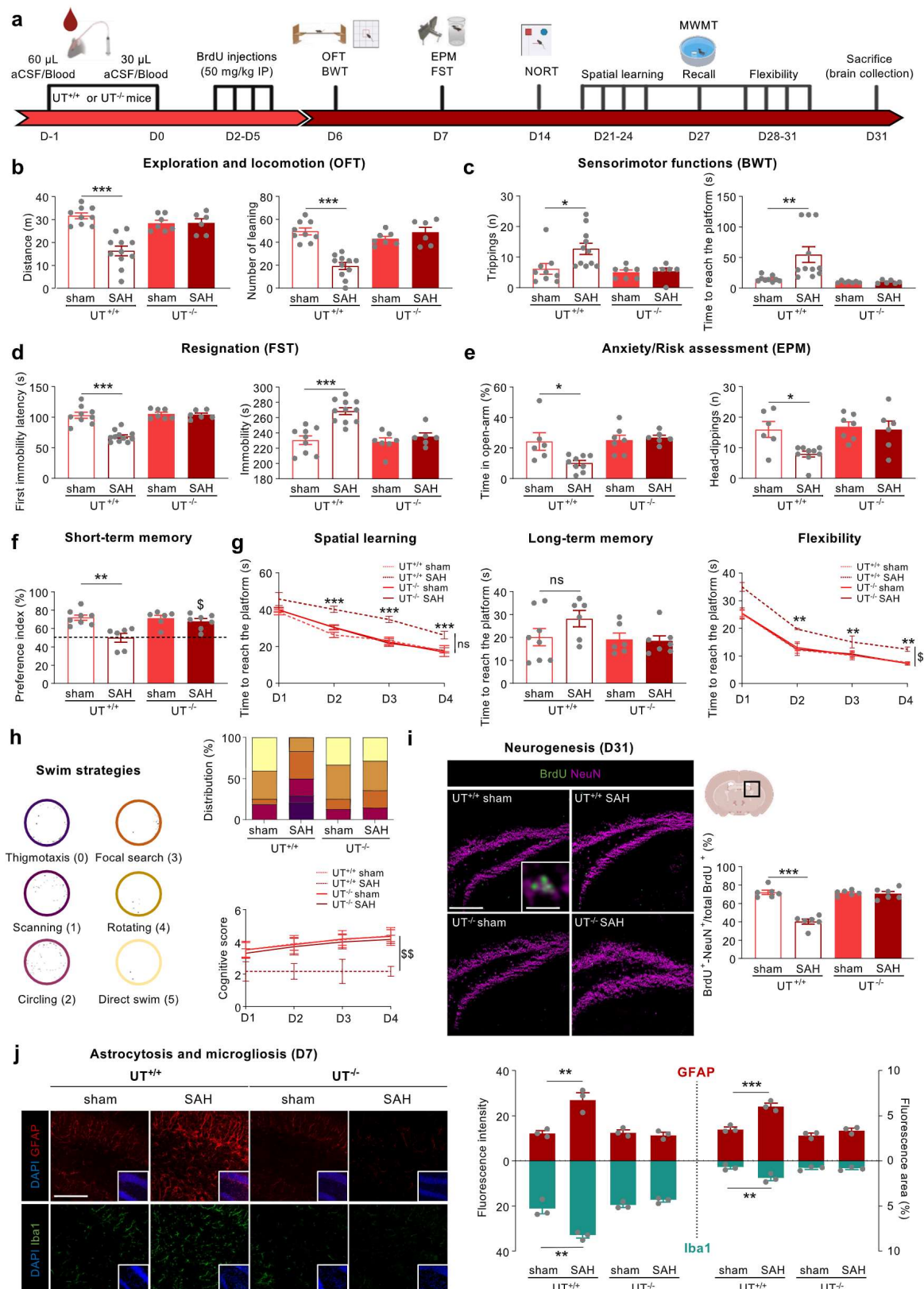
signal (Fig. 4d). To investigate whether ionic or vasogenic edema contributes to the early edema observed, AQP1/4 labeling intensity on D1 was determined by immunohistochemistry. $UT^{+/+}$ SAH mice exhibited a marked increase in AQP1 expression, particularly in the choroid plexus, which was correlated with the ventricular area (r_s=0.860, $p = 0.0000002$) and AQP1 expression was also detected in cortical

microvessels (lectin[+]) (Supplementary Fig. 7a). Additionally, the intensity of AQP4 labeling was increased along the cortical capillaries and in the interhemispheric area containing pia arteries and astrocytic end-feet (GFAP[+]) exclusively in $UT^{+/+}$ SAH mice (Supplementary Fig. 7b), indicating the presence of concurrent ionic and vasogenic edema. To connect early brain edema with the localization of potential

Fig. 2 | The urotensinergic system relays SAH-induced behavioral deficits, neurogenesis, and glial and microglial reactivity post-SAH. a Timeline of the SAH model of double injection of blood into the cisterna magna of UT$^{+/+}$ and UT$^{-/-}$ mice, BrdU injections and behavioral testing before brain collection. OFT, open field test; BWT, beam walking test; EPM, elevated plus maze; FST, forced swim test; NORT and novel object recognition test; MWMT, Morris water maze test. **b–g** Evaluation of exploration and locomotion in OFT (**b**), sensorimotor function in BWT (**c**), resignation in FST (**d**), anxiety and risk assessment in EPM (**e**), short-term memory in NORT (**f**) (**b–e**, $n = 6$–10/condition; f, $n = 6$-8/condition. Values are expressed as the mean ± SEM. *$P < 0.05$; **$P < 0.01$; ***$P < 0.001$ (two-way analysis of variance (ANOVA), Bonferroni's correction). **g** Spatial learning (D21 to D24), long-term memory (D27) and flexibility (D28 to D31) post-SAH in MWMT. **h** Left, swim strategies post-SAH. Each training trial was scored such that more efficient strategies received higher scores, as indicated in parentheses. Right, distribution of search swim strategies during each trial for the 4 days of learning as stacked area percentage recognized by color codes. Cognitive scores during the 4 days of learning correspond to the mean scores attributed to swim strategies (**g**, **h**, $n = 6$–8/condition). Values are expressed as the mean ± SEM. ns, non-significant; \$$P < 0.05$; \$\$$P < 0.01$ (three-way analysis of variance (ANOVA), Bonferroni's correction) illustrating the effect of the SAH in UT$^{+/+}$ mice compared to the three other groups in spatial learning, flexibility and cognitive score). ns, non-significant (two-way analysis of variance (ANOVA), Bonferroni's correction in long-term memory. **i** Quantification of neurogenesis in the hippocampal dentate gyrus in aCSF- and blood-injected UT$^{+/+}$ and UT$^{-/-}$ mice at D31 postsurgery by measuring the BrdU$^+$ (green)/NeuN$^+$ (magenta) ratio ($n = 6$). Scale bar = 200 μm. Zoomed scale bar = 10 μm. Values are expressed as the mean ± SEM. ***$P < 0.001$ (two-way analysis of variance (ANOVA), Bonferroni's correction). **j** Astrogliosis and microgliosis at D7 postsurgery, respectively, quantified by labeled GFAP (red, upper plot) and Iba1 (green, lower plot) intensity (left plot) and area (right plot) ($n = 3$/condition). Scale bar = 100 μm. Values are expressed as the mean ± SEM. **$P < 0.01$, ***$P < 0.001$ (two-sided two-way analysis of variance (ANOVA), Bonferroni's correction). Source data are provided as a Source Data file. **a**, **i** created with BioRender.com released under a Creative Commons Attribution-NonCommercial-NoDerivs 4.0 International license (https://creativecommons.org/licenses/by-nc-nd/4.0/deed.en).

---

blood clots, we immunolabeled fibrinogen deposits on brain slices from UT$^{+/+}$ and UT$^{-/-}$ mice. Large fibrinogen clots were detected on D1, indicating the presence of coagulated blood within some striatal vessels and along ventricular walls in close contact with ependymal cells (Supplementary Fig. 7c); these features were not observed in UT$^{-/-}$ mice.

We then used fast ultrasound imaging (fUS) to map the brain vasculature at microscopic resolution (Fig. 4e). Interestingly, UT$^{+/+}$ SAH mice displayed reduced blood perfusion at the pial and main large arteries of the circle of Willis and penetrating arterioles on D1 and D7 (Fig. 4e). These data indicate that SAH alters the permeability of penetrating arterioles through a UT-dependent process that involves endothelial activation or inflammation. Immunodetection results revealed a parallel increase in fibrin deposition in lectin$^+$ MCA major branches and capillaries (Fig. 4f) and increased cleaved caspase-3 levels in cortical microvessels (Fig. 4g) of UT$^{+/+}$ SAH mice on D7. This same pattern of expression was observed in capillaries of the hippocampal dentate gyrus of UT$^{+/+}$ SAH mice and was associated with reduced microvascular density (Supplementary Fig. 8a, b). These alterations in blood vessel homeostasis were not observed in UT$^{-/-}$ SAH mice, indicating that UT plays a key role in microvessel inflammatory and apoptotic processes that lead to reduced perfusion after SAH.

Given that cerebral blood flow depends on the vessel and microvessel structural architecture, but also on the vasomotricity associated with neurovascular unit functioning, we then evaluated neurovascular coupling as reference to the adjustment of local perfusion to neuronal activity. We thus used fUS to observe cerebral blood volume (CBV) in the barrel cortex during whisker stimulation[40,41]. After SAH, increased UT expression was detected in the barrel cortex (Supplementary Fig. 9a and b). We observed a dramatic decrease in whisker stimulation-induced increased CBV on D1 and D7 in UT$^{+/+}$ mice compared to UT$^{+/+}$ SAH mice (Supplementary Fig. 10a). Neurovascular coupling in UT$^{-/-}$ mice subjected to SAH was statistically less impaired than that in UT$^{+/+}$ SAH mice (Supplementary Fig. 10b). These findings demonstrate the major role of UT in the cerebral vascular inflammatory reaction, the development of brain edema and cerebral blood flow, and the partial contribution of UT in the dysfunction of hyperemia consecutive to SAH.

SAH-mediated early hypoxia-inducible factor-1α (HIF-1α) and UT expression in leptomeningeal fibroblasts trigger CVS

To comprehensively delineate the spatiotemporal expression of UT following SAH, we investigated UT expression using β-Gal reporter immunolabeling at D1 (Supplementary Fig. 11) and UT direct expression at various time points (Fig. 5a) postinjury. In UT$^{+/+}$ mice, UT staining was discernible in leptomeningeal fibroblasts stained by

immunohistochemical analysis of ERTR7 at D1 and progressively decreased until D7 (Fig. 5a, b), here confirming the expression of UT in fibroblasts exclusively in SAH condition as early as D1 postbleeding. Blood content and clots may lead to oxygen deficiency in the subarachnoid space mimicking hypoxia. We then measured the expression of hypoxia-inducible factor-1α (HIF-1α) in the leptomeningeal compartment of both UT$^{+/+}$ and UT$^{-/-}$ mouse brains subjected to SAH. HIF-1α expression was evident in leptomeningeal fibroblasts (labeled by an anti-AKAP12 antibody) in all SAH mice since D1 (Fig. 5c). The administration of siRNA targeting HIF-1α (siHIF-1α) (Fig. 5d) resulted in decreased levels of both HIF-1α and UT in UT$^{+/+}$ SAH mice compared to SAH mice receiving siCTRL (Fig. 5e). At D7, HIF-1α stabilization or expression in MCA was exclusively detected within UT$^{+/+}$ SAH mice, and the lumen area/wall thickness ratio decrease after SAH in siCTRL sham mice, was not detected in siHIF-1α SAH mice (Fig. 5f). These suggest that CVS depends on the HIF-1α-relaying mechanisms consecutive to SAH.

Oxygen radical-dependent pathways[42] may be involved in the blood and hemoglobin (Hb) impact on vasospasm, we thus directly injected Hb into the cisterna magna in place of blood. While cisternal injection of Hb alone did not induce CVS (Supplementary Fig. 12a and b), the combined administration of Hb and UII induced CVS in the MCA at D7 (Supplementary Fig. 12c). Subsequently, we coadministered the drug indirectly stabilizing HIFs VH298 with UII (Fig. 5g), which resulted in elevated UT expression at D1 (Fig. 5h) and evident CVS at D7 (Fig. 5i). We here confirmed in cultured meningeal fibroblasts exposed to 1% O$_2$ (hypoxia) for 72 h (Supplementary Fig. 13a) or treated with VH298 (10 μM) for 24 h (Supplementary Fig. 13b, c) a drastic expression of UT guided by hypoxia and HIF-1α. Together, these results indicate that SAH (or Hb within blood) promotes early HIF-1α stabilization in the leptomeningeal cell compartment leading to UT expression and subsequent CVS in the presence of UII in the subarachnoid space.

Leptomeningeal macrophages express UT and control cerebral vasospasm and behavioral deficits following SAH

In our SAH mouse model, the early HIF-1α-induced UT expression in leptomeninges appears as an essential event for neuroinflammation but also CVS and cognitive deficits. As intermediate contributor, CAM composed of pial, and possibly arachnoid, macrophages within the leptomeninges (MΦ) and perivascular macrophages (PvMΦ) have already been associated with endothelial dysfunction and abnormal vasoconstriction in hypertension[43,44], or more recently in CVS and poor outcome in a preclinical model of SAH[45]. We investigated the role of MΦ and PvMΦ in CVS and associated behavioral abnormalities following SAH and UT expression in MΦs was characterized in UT$^{+/+}$ mice
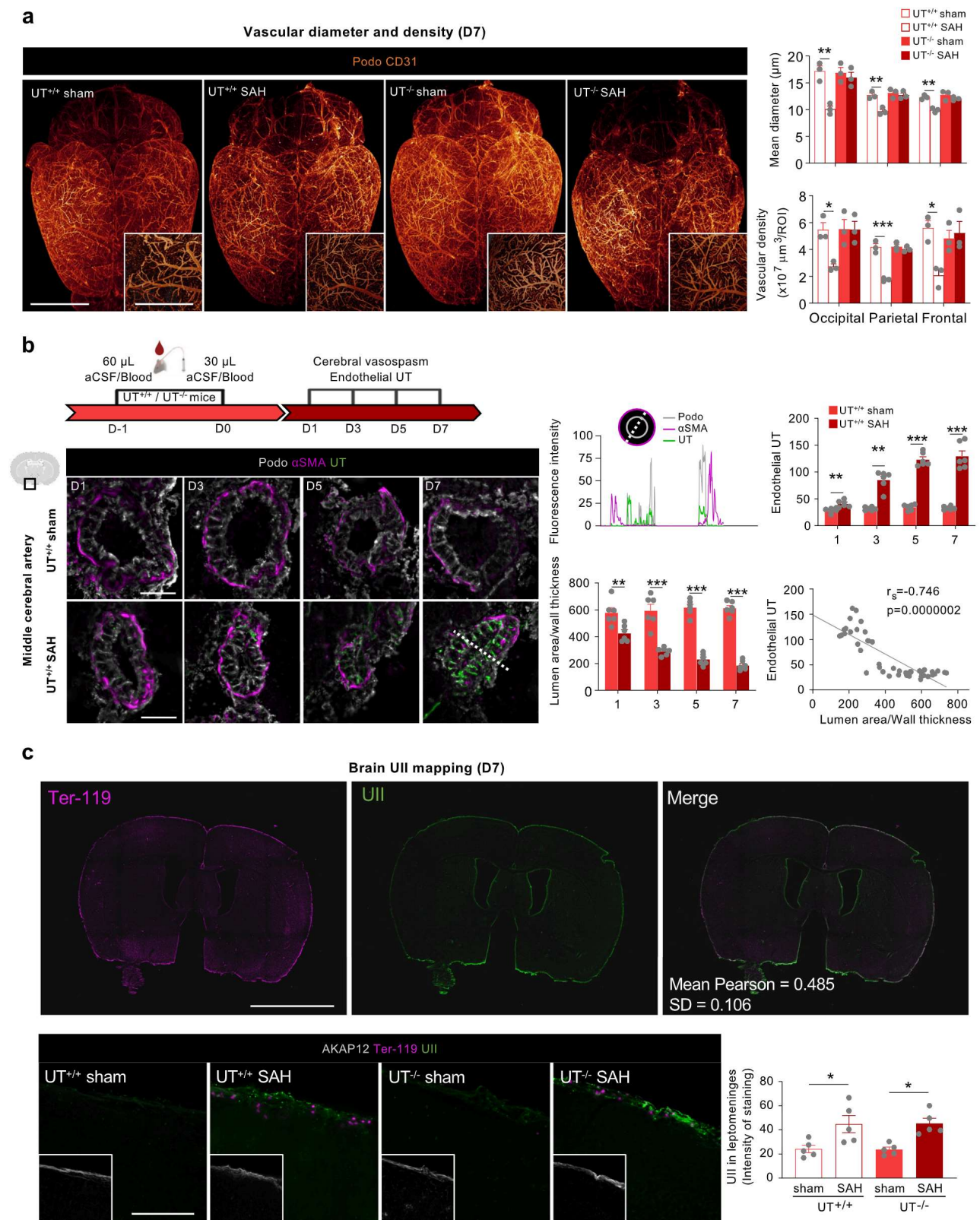
from D1 to D7. CAMs stained by an antibody directed against F4/80, colonized lectin[+] leptomeninges, and perivascular areas at D1 (Fig. 6a and Supplementary Fig. 14a, b), and UT expression was observed on D3 (Supplementary Fig. 14c), as confirmed through both flow cytometry and immunohistochemistry analyses (Fig. 6b, c). To assess the impact of PvMΦs on CVS post-SAH, we specifically depleted leptomeningeal MΦs and PvMΦs using clodronate liposome (CLO) directly injected in

the CSF (Fig. 6d, e), which had no impact on microglia (Supplementary Fig. 15a). Specific PvMΦ depletion did not prevent increases in the intensity of Iba1 immunolabeling or the GFAP[+] signal in the glia limitans at D7 (Supplementary Fig. 15a, b). However, depletion of PvMΦs in SAH mice led to reduced VCAM-1 expression in cortical capillaries, preventing CVS (Fig. 6f and Supplementary Fig. 15c). Notably, PvMΦ depletion in SAH mice resulted in impaired exploratory and locomotor

Fig. 3 | **The onset of SAH initiates UT/β-galactosidase expression in the brain vascular network of UT$^{+/+}$ or UT$^{-/-}$ mice. a** Immunolabeling of Podo$^+$/CD31$^+$ brain vessels (glow dark) from a transparent sham and SAH UT$^{+/+}$ and UT$^{-/-}$ brain generated by iDISCO + . Scale bar = 1 mm. Quantification of mean diameter and vascular density in three ROIs taken from occipital, parietal and frontal cortex areas ($n = 3$/condition). Values are expressed as the mean ± SEM. *$P < 0.05$; **$P < 0.01$; ***$P < 0.001$ (two-sided two-way analysis of variance (ANOVA), Tukey's correction). **b** Timeline of SAH surgery and kinetic analysis of specific endothelial UT expression and cerebral vasospasm. Immunolabeling of middle cerebral artery (MCA) endothelium (podo$^+$, white) and smooth muscle cells (αSMA$^+$, magenta) from D1 to D7 in UT$^{+/+}$ sham and SAH mice showing the kinetics of UT expression (green) from D1 to D7. Quantification of CVS by measuring lumen area/wall thickness ratio (left plot) and UT intensity (right plot). UT is observed in the Podo$^+$ endothelium and not in the αSMA$^+$ layer in the MCA of Blood UT$^{+/+}$ mice.

Spearman test showing a correlation between vasospasm and endothelial UT expression in the MCA ($n = 6$/condition). Values are expressed as the mean ± SEM. **$P < 0.01$; ***$P < 0.001$ (normally distributed, comparison of two groups, unpaired two-sided t-test). **c** Brain mapping from coronal (bregma 0.14 mm) slices of red blood cells immunolabeled by anti-ter-119 (magenta) and UII (green) of SAH UT$^{+/+}$ mouse brain at D1 ($n = 3$). Scale bar = 1 mm. Immunolabeling of ter-119$^+$ red blood cells (magenta) and UII (green) in AKAP12$^+$ (gray) leptomeninges in sham and SAH UT$^{+/+}$ and UT$^{-/-}$ mice at D1. Scale bar = 50 μm. Histogram of quantification of UII intensity in AKAP12$^+$ area ($n = 5$/condition). Values are expressed as the mean ± SEM. *$P < 0.05$, **$P < 0.01$, ***$P < 0.001$ (two-sided two-way analysis of variance (ANOVA), Bonferroni's correction or Spearman's correlation). Source data are provided as a Source Data file. **b** created with BioRender.com released under a Creative Commons Attribution-NonCommercial-NoDerivs 4.0 International license (https://creativecommons.org/licenses/by-nc-nd/4.0/deed.en).

activities, as well as reduced performance in sensorimotor function and short-term memory at D7 (Fig. 6g).

To further explore the contribution of UT expression in CAMs to vascular complications post-SAH, QD655$^+$-labeled differentiated bone-marrow-derived macrophages (BMDMs) from UT$^{+/+}$ (MΦ UT$^{+/+}$) or UT$^{-/-}$ mice (MΦ UT$^{-/-}$) were injected on D-4 (before SAH) in mice previously treated with CLO (Fig. 7a, b). QD655$^+$ staining was detected in leptomeningeal Φs and PvMΦs on D3 (Fig. 7c, d and Supplementary Fig. 16). UT expression was detected in the lectin$^+$ endothelial and F4/80$^+$ myeloid compartments, but CVS was detected only after UT$^{+/+}$ MΦ repletion under SAH conditions (Fig. 7e). Repletion of UT$^{+/+}$ MΦs was associated with IL-6 expression in F4/80$^+$ MΦs in contact with the lectin$^+$ compartment of MCAs at D3, and UT-dependent IL-6 production was found to correlate with CVS (Fig. 7f). Moreover, UT$^{+/+}$ SAH mice injected with UT-expressing QD655$^+$ MΦs showed increased production of reactive oxygen species (ROS) (as measured by DHE staining), which colocalized with QD655$^+$ cells surrounding lectin$^+$ vascular structures (Supplementary Fig. 17). This finding suggests that UT expression in leptomeningeal MΦs and PvMΦs induces CVS through IL-6 and ROS production, thus contributing to poor neurological outcomes. Exploratory behavior, sensorimotor function, and index preference in the novel object recognition test were drastically diminished in SAH UT$^{+/+}$ mice administered UT$^{+/+}$ MΦs and, to a lesser extent, in SAH mice administered UT$^{-/-}$ MΦ compared to sham mice administered UT$^{+/+}$ or UT$^{-/-}$ MΦs (Fig. 7g).

Leptomeningeal glia limitans reactivity and delayed neuroinflammation are facilitated by UT, bypassing MΦs

We observed an increase in GFAP intensity in astrocytes of the glial limitans adjacent to the leptomeninges on D1 in SAH mice expressing UT (Fig. 8a). To investigate whether UT-induced astrogliosis originates from pial MΦs and/or leptomeningeal fibroblasts, MΦs were depleted in UT$^{+/+}$ and UT$^{-/-}$ mice before SAH induction. Subsequently, the MΦ population was replenished with QD$_{655}$-labeled MΦs derived from UT$^{+/+}$ mouse BMDMs. Surprisingly, F4/80-expressing MΦs were identified in leptomeningeal and perivascular cortical areas on D1 (Fig. 8b) in all mice, and expression of the astrogliosis marker GFAP was induced at D1 and D7 in ERTR7$^+$ leptomeninges and at D7 in the hippocampal fissure only in UT$^{+/+}$ mice, with UT$^{+/+}$ MΦ repletion (Fig. 8c, d). Notably, MΦs are essential for mediating delayed vascular consequences, such as the CVS observed on D7, in both UT$^{+/+}$ and UT$^{-/-}$ mice in which the MΦ population was reconstituted with UT$^{+/+}$ MΦs (Fig. 8e).

Therefore, UT expression in the leptomeningeal layers promotes astrogliosis in a MΦ-independent manner. Moreover, UT expression in PvMΦs alone is necessary and sufficient to induce CVS in UT$^{-/-}$ mice. Interestingly, behavioral analyses of UT$^{-/-}$ mice reconstituted with UT$^{+/+}$ MΦs after SAH revealed only alterations in spontaneous activity, exploration, and sensorimotor function (Fig. 8f) while significant differences were found between UT$^{+/+}$ SAH and UT$^{-/-}$ SAH + UT$^{+/+}$ MΦs

behavioral parameters. The absence of behavioral defects in UT$^{-/-}$ mice after SAH and UT$^{+/+}$ MΦ reconstitution emphasizes that MΦs expressing UT contribute to CVS and to the observed deficiencies in exploration and sensorimotor activities.

Human UT couples the Gq/PLC/PKC pathway to mediate SAH-induced vasospasm, astrogliosis associated with leptomeninges, and behavioral impairment

Our current data highlight that UII, UT or UT-associated signaling pathways mediate CVS, proinflammatory pial and PvMΦs, and leptomeningeal cell responses, thus UT could therefore represent a new therapeutic target in SAH. We therefore aimed to first understand the signaling pathways linked to the known Gq and Gi/o couplings of UT potentially involved in the cerebral consequences of SAH, and then to select the best therapeutic tool toward the UT-involved signaling. we subjected humanized mice expressing UT (UT$^{h/h+}$) to SAH before assessing potential therapeutic interventions (Supplementary Fig. 18). Human UT (hUT) overexpression in the ERTR7$^+$ leptomeningeal fibroblasts and in the podocalyxin$^+$ vascular compartment was observed in UT$^{h+/h+}$ mice on both D1 and D7 (Supplementary Fig. 19). To confirm the efficacy of UT/PLC/Ca^{2+} coupling in our model, cultured human and murine meningeal fibroblasts from UT$^{h+/h+}$, UT$^{+/+}$, and UT$^{-/-}$ mice were exposed to the HIF-1α stabilizer VH298. These VH298-treated fibroblasts exhibited a Ca^{2+} response to increasing concentrations of human UII (hUII) (10^{-11}-10^{-6} M) (Supplementary Fig. 20a). Conversely, pretreatment of UT$^{h+/h+}$ meningeal cells with VH298 and incubation with the Gq inhibitor YM-254890 significantly decreased both the affinity and efficacy of the response to hUII (Supplementary Fig. 20b). Importantly, the Gi/o peptide inhibitor PTX did not counteract the hUII-induced Ca^{2+} response, indicating that in the early stages following SAH, UT can recruit the Gq/PLC/Ca^{2+} pathway in the leptomeninges. Note that the selectivity of YM-254890 and PTX for Gq and Gi/o was verified and confirmed by means of bioluminescence resonance energy transfer-based and a homogeneous time-resolved fluorescence assays (Supplementary Fig. 21a, b). Additionally, we investigated the impact of the Gq/PLC/PKC or Gi/o/PKA cascade in vivo during the early (D1) and delayed (D7) periods post-SAH in UT$^{h+/h+}$ mice (Fig. 9a). At D1, SAH increased p-PKC immunostaining in ERTR7$^+$ leptomeningeal fibroblasts, while p-PKA levels remained unchanged (Fig. 9b). At D7, SAH-induced p-PKC immunolabeling was observed in the lectin$^+$ MCA compartment and in F4/80$^+$ PvMΦs; this effect was not observed in the presence of YM-254890 or U73122 (Fig. 9c). Notably, CVS of the MCA was measured after SAH and correlated with p-PKC levels in PvMΦs. Intracisternal administration of YM-254890 or U73122 prevented the occurrence of CVS and sensorimotor deficits post-SAH (Fig. 9d, e), supporting the hypothesis that Gq/PLC/PKC signaling has a significant impact on these factors. Subsequently, we compared the effects of hUII on HEK293 cells expressing hUT with those of the biased ligand urantide and the selective nonpeptide antagonists palosuran and GSK1562590. hUII, urantide, palosuran and GSK1562590 treatment

Article
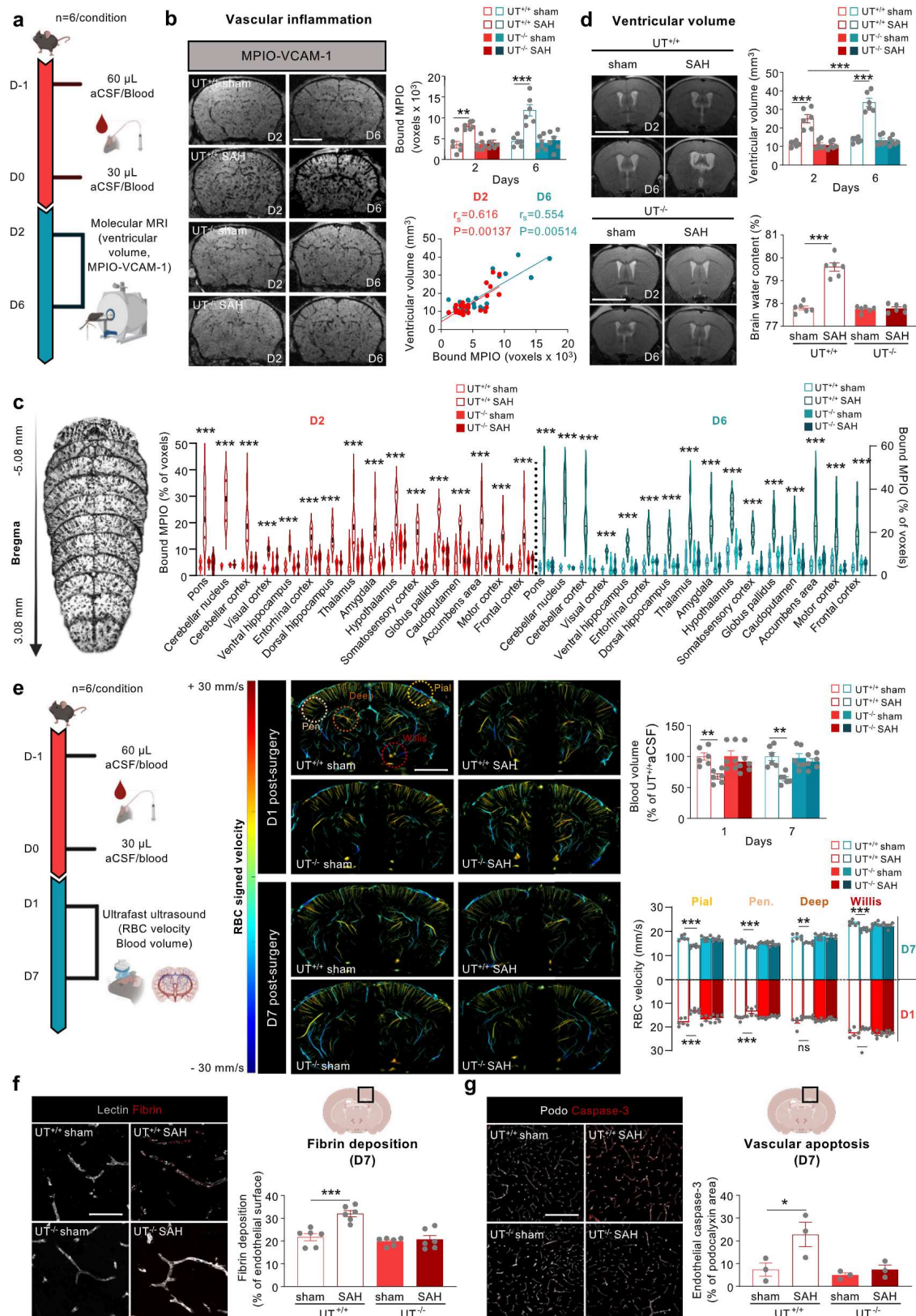
resulted in concentration-dependent effects on UT/Gi1, Gi2, Gi3, GoA, GoB, Gz, Gq coupling, IP1 production, and Ca²⁺ mobilization (Supplemental Table 1 and Supplemental Fig. 22). GSK1562590 induced a significant rightward shift in hUII activation of Gi2, Gi3, GoA, GoB, and Gz and prevented the recruitment of Gi1, Gq, and β-arrestin 1 and 2, as well as Ca²⁺ mobilization, indicative of active UT antagonism

(Supplemental Table 1 and ig. 10a–e). Palosuran appeared to be less effective or inefficient at antagonizing the effects of hUII on various pathways (Fig. 10a–e). Urantide, a biased ligand, caused a significant rightward shift in the hUII dose-response curves, particularly for UT-induced Gi1, Gi2, Gi3, Gq, β-arrestin 1 and 2, and Ca²⁺ mobilization (Supplemental Table 1 and Fig. 10a–e). In vivo, in UT^{h+/h+} mice,

Fig. 4 | UT drives brain vascular disorders associated with SAH. a Timeline of SAH surgery and molecular MRI coupled with intravenous injection of MPIO-anti-VCAM-1. **b, c** Representative T2*- (**b**) and T2- (**c**) weighted MRI brain images in sham and SAH UT^{+/+} and UT^{-/-} mice. **b** Representative histograms of voxel density within a brain from D2 to D6 after SAH post-MPIO injection. Histogram of quantification of brain water content in sham and SAH UT^{+/+} and UT^{-/-} mice at D1 ($n = 6$/condition). Values are expressed as the mean ± SEM. ***$P < 0.001$ (two-sided two-way analysis of variance (ANOVA, Bonferroni's correction or Spearman's correlation).
c Representative T2*-weighted MRI brain images in SAH UT^{+/+} and UT^{-/-} mice from bregma −5.88 mm to 3.08 mm and histograms of bound MPIO by measuring voxel density in each brain structure in sham and SAH mice at D2 and D6 ($n = 6$/condition). **d** Quantification of ventricular volume by measuring white voxel density (right plot, $n = 6$/condition) from D2 to D6 images (upper panel) and brain water content (lower panel) in sham and SAH UT^{+/+} and UT^{-/-} mice. **e** Timeline of SAH surgery and fUS methodology to measure red blood cell (RBC) velocity and blood volume at D1 and D7. Illustrations depicting signed RBC velocity on a cross-section of mouse brains (bregma -1.82 mm) from aCSF and Blood UT^{+/+} and UT^{-/-} mice at D1

(upper panel) and D7 (lower panel) postsurgery. Quantification of blood volume (upper right panel) and RBC velocity (lower right panel) changes at D1 and D7 postsurgery in pial, deep or Willis circle arteries and penetrating (Pen) arterioles. Scale bar = 2 mm. **f** Immunolabeling and quantification of fibrin (magenta) in lectin[+] (green) cortical vessels in sham and SAH from UT^{+/+} and UT^{-/-} mice at D7 ($n = 6$/condition). Scale bar = 50 μm. **g** Immunolabeling of podo[+] (white) and caspase-3 (red) to quantify cortical endothelial apoptotic events in aCSF and blood from UT^{+/+} and UT^{-/-} mice at D7 ($n = 6$/condition). **c–f** Values are expressed as the mean ± SEM. *$P < 0.05$; **$P < 0.01$; ***$P < 0.001$ (two-sided two-way analysis of variance (ANOVA) with repeated measures, Bonferroni's correction). Quantification of activated caspase-3 intensity in podo[+] endothelial components, ($n = 3$). Scale bar = 100 μm. Values are expressed as the mean ± SEM. *$P < 0.05$ (two-sided two-way analysis of variance (ANOVA, Tukey's correction). Source data are provided as a Source Data file. **a, e, f, g** created with BioRender.com released under a Creative Commons Attribution-NonCommercial-NoDerivs 4.0 International license (https://creativecommons.org/licenses/by-nc-nd/4.0/deed.en).

---

intracisternal coinjection of urantide, palosuran, or GSK1562590 was compared to the injection of aCSF or blood; the three compounds prevented CVS in the MCA of SAH mice (Fig. 10f, g). Furthermore, exploration and sensorimotor dysfunction induced by SAH was also prevented by treatment with all three UT ligands at D7 (Fig. 10g). Together, these data suggest that UT-biased ligand urantide or GSK1562590 and palosuran antagonists could be promising candidates for clinical trials targeting neuroinflammation, CVS and behavioral disorders post-SAH.

Discussion

After aneurysmal SAH, initial bleeding within the cortical surface and ventricles often leads to major complications, such as EBI involving hydrocephalus and dysregulated cerebral blood flow, ultimately resulting in devastating DCI[46]. Despite intense efforts and research in preclinical field, and the number of clinical trials, there are no treatments to prevent these events at the time of occurrence or to cure them[47]. The therapeutic lack of efficiency towards CVS or SAH patient outcome reflects the incomplete understanding of the physiopathological processes responsible for these delayed neurological complications. The aim of the present study was to better decipher key early mechanisms occurring in the leptomeninges covering brain surface, the first territory reached by blood components in SAH, and identify the main contributors connecting leptomeninges, neuroinflammation and CVS. The objective was to characterize and test a new receptor target, the UT receptor of the vasoactive peptide UII and its associated pathways in this cascade of event, to counteract or avoid SAH-associated long-term cognitive impairment. Here we have shown that genetic and pharmacologic neutralization of the urotensinergic system involved in early leptomeningeal glia limitans reactivity, and vascular and neuroinflammatory processes mediated by CAMs and more particularly PvMΦs could dampen cerebral vasospasm and behavioral disorders following SAH in a mild mouse model of SAH.

Several potential therapeutic strategies, including vessel occlusion using antiplatelets or fibrinolytic agents and the use of CVS inhibitors such as the ETA antagonist clazosentan or the statin simvastatin, have been identified in preclinical studies and are being explored in clinical trials[17,48–50]. The UII receptor UT is selective for UII-like peptides, which are known for their potent vasoconstrictive properties, similar to ET-1, and their role as chemoattractants in inflammatory diseases and cancer[22,25]. The UII/UT system, which is similar to yet distinct from other vasoactive GPCRs, exhibits pleiotropic functions. Indeed, UT originally exhibits pleiotropic functions by coupling not only Gq and PLC/PKC/Ca^{2+} signaling but also Gi/o and G13 and NF-κB or RhoA/Rock pathways[51–53], suggesting possible inflammatory effects of this understudied receptor[51–53]. Our investigation revealed increased UT

expression in various brain structures post-SAH, which was particularly evident in pia mater fibroblasts adjacent to astrocyte endfeet and in endothelial cells from main cerebral arteries, capillaries and microvessels. This result contrasts with the low UT expression levels observed in the noninjured brain. We confirmed UII expression in the endothelial layer of cerebral arteries, consistent with previous findings[54–57], but we also observed a spatial correlation between erythrocytes and UII expression in leptomeningeal cells in the early stage post-SAH, suggesting that blood clots containing UII are in contact with the meninges, potentially activating UT. Previous studies established circulating UII concentrations ranging from pg/mL to ng/mL[58,59]. Importantly, we previously demonstrated no alteration of the mean level of UII in plasma of SAH patients from D1 to D10, while symptomatic CVS patients exhibited the highest level of UII in plasma[21], underlining the contribution of UT becoming actionable after SAH, and activated by UII present in blood. Here we provide evidence that blood or Hb itself or erythrocyte metabolite compounds in the subarachnoid space is responsible for UT gene expression in meningeal fibroblasts. Accordingly, it has been shown that prolonged intrathecal infusion with Hb can mimic SAH-induced small vessel spasms, CVS and locomotor disorders[60], and that ROS levels found in CSF resulting from autoxidized Hb correlates with the occurrence of CVS and DCI in SAH patients[61], thus all suggesting a link between blood/Hb (and ROS), hypoxia and the expression of UT. In line with clinical studies showing that hypoxia-related factors were detectable during EBI after SAH[62–64], we here showed that blood stimulates HIF-1α expression/stabilization in the leptomeningeal layers at D1 and in the MCA compartment at D7. This hypoxic marker may result from hypoxia declaring within minutes after bleeding due to blood, erythrocyte hemolysis leading to iron production through the oxygen enzymatic dependent reaction consuming O_2[64] and Hb-oxydizing products. Moreover, we highlight the presence of erythrocytes along perforating arteries and in the skull meaning that arachnoid granulations can be obstructed by blood clots, potentially involved in the reduction of cerebral blood flow and draining leading to hydrocephalus[65]. Thus in the context of SAH-induced impairment of CSF absorption and clearance via the glymphatic system[66], we assume that hypoxic CSF, and Hb-oxidizing products including ROS[67] potentially stimulate pathways of HIF-1α stabilization, that would in turn binds the UT gene promoter[68] in ERTR7^{+} fibroblasts, then leading in a HIF-1α-dependent or independent way to increased UT endothelial expression in capillaries and vessels. Furthermore, our results revealed that early brain cytotoxic and vasogenic edema exclusively occurred in SAH mice with increased UT expression, suggesting connection among UT and edema as part of SAH-induced EBI and delayed poor neurological outcomes associated with SAH. This finding aligns with clinical studies emphasizing the significance of the initial bleeding event and EBI in SAH describing a

Article
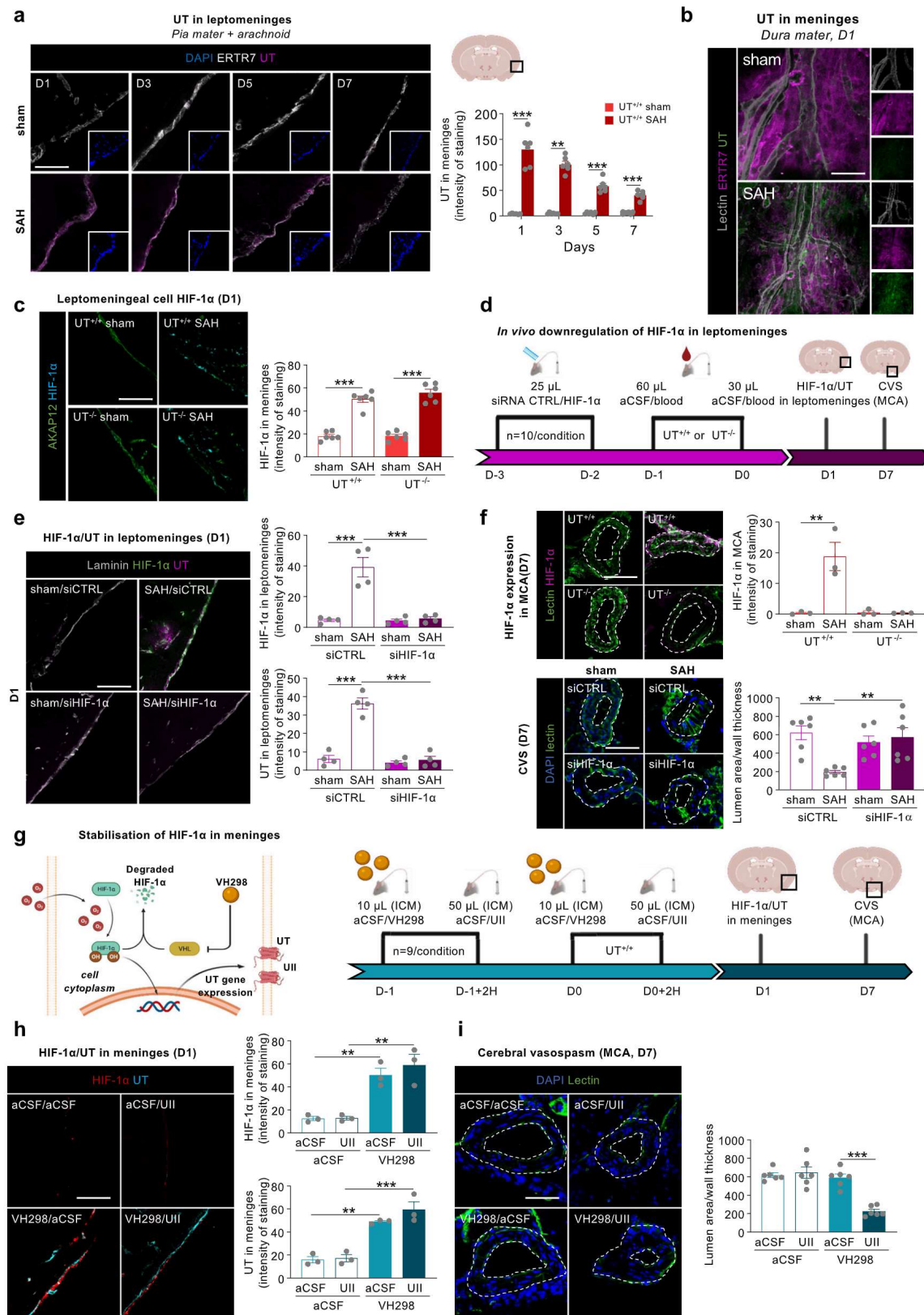
link between CSF Hb content in CSF and clinical DCI[69], cortical iron and cognitive outcome[70], predictive role of CSF superoxide dismutase with poor neurological outcome of SAH patients[71,72]. Overall, our data suggest that while the UII/UT system appears to be silent under physiological conditions, UT overexpression post-SAH activated by UII-loaded blood could be the missing link between blood diffusion in the subarachnoid and perivascular spaces and the subsequent cascade of events including microvascular defects, vasospasms of large distant arteries (CVS) and neuroinflammation, and neurobehavioral alterations. Understanding the UT contribution in each mechanism may open avenues for targeted interventions to improve outcomes in SAH patients.

Fig. 5 | HIF-1α stabilization post-SAH induces early expression of UT in lepto-meningeal fibroblasts and late cerebral vasospasm at D7. a Immunolabeling of ERTR7^{+} (white) meningeal fibroblasts of leptomeninges showing UT (magenta) overexpression and DAPI (blue) in SAH compared with sham conditions. Quantification of UT intensity from D1 to D7 in ERTR7^{+} areas ($n = 5$). Scale bar = 50 μm. **b** Immunolabeling of the dura mater showing UT (green) overexpression in SAH compared to sham conditions at D1 in ERTR7^{+} (magenta) meningeal fibroblasts bordering dural lectin[+] (gray) vessels ($n = 3$/condition). Scale bar = 50 μm. **c** Immunolabeling of leptomeninges showing HIF-1α (cyan) overexpression at D1 in AKAP12^{+} (green) meningeal fibroblasts in SAH compared with sham conditions. Quantification of meningeal HIF-1α intensity in AKAP12^{+} areas ($n = 6$). Scale bar = 50 μm. **d** Timeline of intracisternal injections of siRNA targeting HIF-1α gene expression one day before SAH surgery. **e** Immunolabeling of leptomeninges showing at D1 HIF-1α (green) and UT (magenta) expression in SAH compared to sham conditions in mice pretreated with siCTRL or siHIF-1α in laminin[+] (gray) meningeal fibroblasts. Quantification of HIF-1α (upper panel) and UT (lower panel) intensity in laminin[+] areas ($n = 4$). Scale bar = 50 μm. **f** MCA delimited via lectin[+] (green) and DAPI (blue) staining at D7. MCA lumen area/wall thickness ratio in SAH compared to sham conditions in mice pretreated with siCTRL or siHIF-1α (lower panel). Quantification of the lumen area/wall thickness ratio ($n = 6$). Scale bar = 50 μm. HIF-1α (magenta) expression in peri-MCA in SAH compared to sham UT^{+/+} and UT^{-/-} mice (upper panel). Quantification of perivascular HIF-1α intensity in the MCA ($n = 6$). Scale bar = 50 μm. **g** Timeline of intracisternal injection of aCSF or VH298 prior to intracisternal injection of aCSF or UII. **h** Immunolabeling of HIF-1α (red) or UT (cyan) within leptomeninges at D1 in sham- or VH298-pretreated mice and in the absence or presence of UII. Quantification of HIF-1α (upper panel) and UT (lower panel) intensity in meningeal cells. Scale bar = 50 μm. **i** MCA delineation with lectin (green) and DAPI (blue) staining at D7. Quantification of the lumen area/wall thickness ratio ($n = 3$). Scale bar = 50 μm. **a–i** Values are expressed as the mean ± SEM. *$P < 0.05$; **$P < 0.01$; ***$P < 0.001$ (**a–g**, **i**) Two-sided two-way analysis of variance (ANOVA), Bonferroni's correction). **h** two-sided two-way analysis of variance (ANOVA), Tukey's correction. Source data are provided as a Source Data file. **a**, **d**, **g** created with BioRender.com released under a Creative Commons Attribution-NonCommercial-NoDerivs 4.0 International license (https://creativecommons.org/licenses/by-nc-nd/4.0/deed.en).

Poor neurological outcome and cognitive deficits[73–76], were often assigned to DCI, likely consecutive to CVS. In this study, we established that blood and/or Hb and consecutive increases in HIF-1α concentration led to early UT expression in leptomeningeal cells and cortical and hippocampal capillaries and small vessels which controlled the diminished CBV in microvessels and the occurrence of CVS in large arteries. These observations corroborate previous preclinical studies in which blood evokes a marked increase of cerebral blood flow after blood injection slightly recovering during the course of CVS[77,78] and spasms of pial arteriols exhibiting thrombi[79,80]. Here we show that CVS development involves early UT expression in leptomeninges, glia limitans reactivity and vascular inflammation, as well as platelet aggregation and microvascular apoptosis (Supplemental Fig. 23). Interestingly, as recently reported[81,82], we found a neurovascular uncoupling in the barrel cortex consecutive to SAH indicative of an autoregulation deficit. A primary contribution of Ca^{2+} to the neurovascular unit in astrocytic endfeet has been suggested in SAH Rats[83], but we also highlight that this autoregulation defect is partly dependent on UT, expanding its role to vasomotricity.

Although well known for its cardiovascular effects, the urotensinergic system has recently been reported to play chemoattractant and proinflammatory roles in cancer[26] and septic shock[84], highlighting its versatile nature in pathological situations, depending on the tissue and the situation. This versatility comes from the pleiotropic effects of UT on Gq/11/IP3/Ca^{2+}, Gi/o/PI3K/Akt, and G12/13/Rho/Rock[22]. In the context of SAH, blood stimulates P-PKC rather than P-PKA in ERTR7^{+} leptomeningeal fibroblasts via a Gq/PLC-dependent pathway associated with glia limitans activation. Although it is unclear how this signaling pathway leads to neuroinflammation, hypoxia resulting from ischemic lesions has been shown to decrease the expression of the PKA/PKC scaffold protein AKAP12 in the meninges, directly or indirectly contributing to PKC phosphorylation[85]. UII evokes intracellular Ca^{2+} mobilization in stimulated meningeal fibroblasts through the UT/Gq/11 axis, indicating that in SAH, the UT/Gq/PLC and P-PKC cascades may promote mesenchymal transition and alter the meningeal barrier, potentially contributing to neuroinflammation. The mechanisms and cell types involved in this process may be diverse, but similar to AT1R or PAR1/4[86], UT/Gq signaling components may involve NADPH oxidase, 5-lipoxygenase, PKC, AKT, ROS, and/or NF-κB mediators in smooth muscle cells, fibroblasts, and monocytes/MΦs/microglia[87–90]. An SAH-induced reduction in CBV and endothelial cell adhesion molecule expression allows MΦs and neutrophils to be trapped in the subarachnoid space[91]. Neutrophils, and mainly dura and pia MΦs as well as PvMΦs, may release inflammatory factors or oxidative radicals that contribute to microvascular thrombi as observed in our study. The early post-SAH events observed here included an increase in MΦs expressing UT in the leptomeninges and perivascular space. CLO-induced MΦ depletion in the leptomeninges and perivascular space completely prevented microvascular inflammation and CVS, which attenuates SAH-induced emotional and behavioral deficits. Our findings align with those of a recent study, which showed that CAMs are involved in neuronal injury, inflammation surrounding large arterioles, and microthrombosis after SAH[45]. Here, we used quantum dot-loaded MΦs isolated from UT^{+/+} or UT^{-/-} mice to examine MΦ trafficking post-SAH. Our results indicate that UT is expressed in MΦs only in the presence of blood-induced HIF-1α, leading to ROS production and IL-6 expression. This capacity of UII/UT to activate the NOX-2/NADPH oxidase pathway or stimulate IL-6 secretion in tumoral or endothelial cells[92,93] and the possible NOX2-ROS-mediated IL-6 production in MΦs[94] support SAH-mediated HIF-1α/UT/NOX2/ROS-dependent IL-6 proinflammatory cytokine production in MΦs, which is closely associated with CVS development. Similarly, IL-6 is involved in the pathogenesis of CVS[95] and DCI[96] after SAH in patients, and the IL-6 antagonist tocilizumab appears to be protective in a rabbit SAH model[97]. Our data reveal that UT expression in pial MΦs and PvMΦs causes IL-6 production and CVS, leading to the observed behavioral deficits after SAH.

Although CVS has long been assumed to be entirely responsible for DCI and cognitive deficits after SAH, recent clinical trials have highlighted that CVS is not always associated with poor outcomes[98]. Poor clinical outcomes post-SAH, including cognitive deficits lasting for years, have been associated with the extent of bleeding in the subarachnoid space, EBI, acute hydrocephalus, and new cerebral infarction. In SAH, alterations in various brain regions have been correlated with impaired memory performance. In our study, we propose that the meninges, which are the first brain structures exposed to blood during SAH and project underneath the hippocampal formation in continuity with the choroid plexus, contribute to the observed patient outcomes. Meningeal fibroblast layers expressing UT control astrogliosis and microglial reactivity and extend toward hippocampal fissures to at least partially control neurogenesis. This loss of neurogenesis can be associated with leptomeningeal glia limitans activation and inflammation, microglial reactivity, and oxidative stress in the cortex and hippocampus or with blood–brain barrier disruption. The meningeal niche, comprising neural precursor cells and fractones, plays a role in regulating neurogenesis and spatial learning functions, depending on the inflammatory status of meningeal MΦs. A wide array of post-SAH emotional and cognitive deficits, including activity, emotional reactivity, cognitive score and exploration/attention had been demonstrated UT-dependent but partly mediated by leptomeninges-induced neuroinflammation and IL-6-expressing MΦs leading to CVS (Supplemental Fig. 23). The inflammatory PvMΦs and meningeal MΦs lining the hippocampal dentate gyrus directly
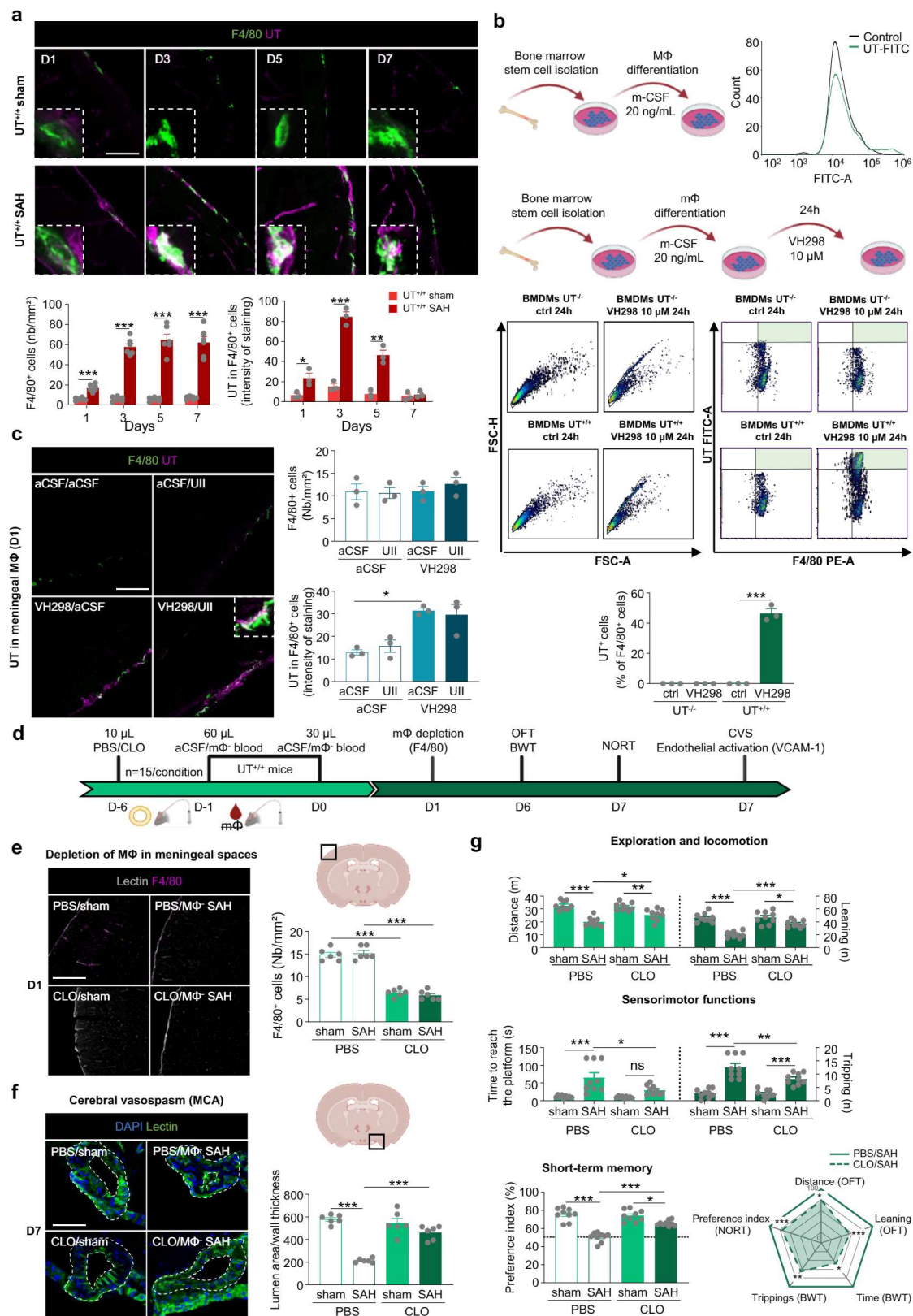
interfere with neurogenic processes. Thus, our results indicate that UT expression is specifically triggered by SAH and is responsible for neurocognitive deficits; thus, further investigation of UT as a target for new therapeutic interventions is warranted.

To validate the therapeutic value of UT and its Gq/PLC signaling, the β-arrestin-biased ligand urantide[51] and the antagonists palosuran

and GSK1562590 were tested on UT Gi1, Gi2, Gi3, Gz, Gq, IP1, GoA, GoB couplings, on Ca^{2+} increase and β-arrestins 1 and 2 recruitment, as well as affinity and efficacy of UII toward hUT expressed on HEK cells. We here prove the partial agonistic impact of urantide on UT G protein couplings, and clinically relevant prevention of the UT-activating Gq/PLC/Ca^{2+} signaling pathway by preincubation with urantide or

Fig. 6 | Leptomeningeal macrophages expressing UT are involved in cerebral vasospasm induced by SAH. a Kinetics of F4/80+ (green) pial MΦ recruitment and UT (magenta) overexpression in leptomeninges from D1 to D7 in SAH compared to sham UT+/+ mice. Quantification of the number of F4/80+ MΦs (left panel, $n = 5$) and UT intensity in F4/80+ cells (right panel, $n = 3$) from D1 to D7. Scale bar = 50 μm. Values are expressed as the mean ± SEM. *$P < 0.05$; **$P < 0.01$; ***$P < 0.001$ (normally distributed, comparison of two groups, unpaired two sided t-test). **b** FACS analysis and gating strategy (upper right quadrant F4/80+ UT+) for bone marrow-derived (in vitro, see Material and Methods) F4/80+ MΦs (BMDMs) obtained from UT+/+ or UT-/- mice and treated or not treated with VH298 (24 h). Quantification of the percentage of UT-expressing cells among total F4/80+ BMDMs ($n = 3$). Values are expressed as the mean ± SEM. ***$P < 0.001$ (two-sided two-way analysis of variance (ANOVA), Tuckey's correction). **c** Immunolabeling of leptomeninges of UT (magenta) and F4/80+ (green) MΦs at D1 in aCSF- or VH298-pretreated mice and in the absence or presence of UII in the subarachnoid space ($n = 3$). Scale bar = 50 μm. Values are expressed as the mean ± SEM. *$P < 0.05$ (two-sided two-way analysis of variance (ANOVA), Tuckey's correction). **d** Experimental timeline of leptomeningeal and PVMΦ depletion by intracisternal injection of clodronate-liposomes

(CLO-lip) before SAH with blood from mice depleted of peripheral MΦs prior to behavioral testing and brain analyses. Values are expressed as the mean ± SEM. *$P < 0.05$; ***$P < 0.001$ (two-sided two-way analysis of variance (ANOVA), Tuckey's correction). **e** Immunolabeling of F4/80+ (magenta) MΦs around lectin+ (white) leptomeningeal and perivascular vessels. Histograms of quantification of the total number of F4/80+ cells at D1 in sham and SAH conditions. **f** Immunolabeling of lectin+ (green) and nuclei by DAPI (blue) in MCA at D7 in PBS-lip and CLO pretreated mice. Quantification of lumen area/wall thickness ($n = 6$). Scale bar = 50 μm. **g** Exploration and locomotion in OFT. Sensorimotor functions in the BWT and preference index in the NORT ($n = 9$/condition). Radar plots illustrating the relative effect of SAH in CLO pretreated mice on performance in OFT, BWT, and NOR test. Each item of the radar represents the mean normalized to CLO pretreated PBS mice. **e–g** Values are expressed as the mean ± SEM. ns=non-significant, *$P < 0.05$; **$P < 0.01$; ***$P < 0.001$. (two-sided two-way analysis of variance (ANOVA), Bonferroni's correction). Source data are provided as a Source Data file. **b, d–f** created with BioRender.com released under a Creative Commons Attribution-NonCommercial-NoDerivs 4.0 International license (https://creativecommons.org/licenses/by-nc-nd/4.0/deed.en).

GSK1562590, in agreement with previous studies[99]. However, only partial UT antagonism was mediated by palosuran, in accordance with the lack of sufficient affinity toward hUT in some in vitro functional assays[100] and the poor clinical efficacy in diabetic nephropathy patients[101]. This last observation fuels the controversy surrounding the in vivo efficacy of the UT antagonist palosuran that may disqualify its clinical use. Based on these observations, urantide, palosuran, and GSK1562590 were tested in vivo on SAH consequences. The most striking observation is that all three UT ligands counteract the impact of blood on CVS, exploration and sensorimotor functions of UT^h+/h+ mice post-SAH (supplemental Fig. 23), suggesting that blocking the action of UII on the UT-Gq/PLC/Ca2+ pathway can prevent major consequences of SAH.

Limitation of the present study

Despite the considerable potential of the urotensinergic system as a new therapeutic target in SAH, several limitations in the present study should be considered. We assessed the UII-relying mechanisms of SAH on behavioral consequences and the efficacy of pharmacologically targeting UT exclusively in male C57Bl/6 mice due to the reproducibility of the SAH model in males, at least in our hands[27,28]. This choice aligns with the recommendations of the European directive (Directive 2010/63/EU) aiming to reduce the number of animals in in vivo experiments. As emphasized in the guidance on Sex and Gender Reporting in Research[102], we acknowledge the underrepresentation of women in clinical research and female animals in experimental protocols, which may have adverse consequences, especially in cardiovascular pathologies and ischemic stroke.

Interestingly, incidental unruptured cerebral aneurysms were found to be more prevalent in females than in males[103], likely due to the inhibitory effect of estrogens on arterial wall cell matrix adhesive properties and proinflammatory reactions. However, sex differences in the incidence of SAH remain controversial. A higher risk for SAH was previously described in postmenopausal females compared with premenopausal ones at the same age, or compared with males in older patients[104]. Additionally, despite several studies showing that sex was not associated with functional status post-SAH[105–107], a recent large panel analysis from the SAH international trialists repository suggested that female sex correlates with worse functional outcomes[108–110]. Therefore, future research on SAH should include female mice to confirm whether macrophages and meningeal inflammation drive SAH behavioral consequences and alter UT targeting as a therapeutic response.

Some terms used here as reference of cerebral vessels or leptomeninges would appear lacking of precision in the identification of the cerebral arteries, arterioles or capillaries, and veins or venules

expressing UT after SAH. Despite important publications of reference to precise cerebral vascular atlas in whole mouse brain[111] or the mapping of fine vascular architecture and plasticity after stroke[112], the panel of specific markers and the spatial resolution of imaging methods used here did not allow the cerebral vascular system to be traced, not only arteries and main branches, capillaries, and arterioles, but also veins and venules, in which UT could be expressed after SAH.

Another limitation stems from the SAH rodent models used in the present study, which may not entirely recapitulate the course of mechanisms and symptomatology observed in SAH in humans. In patients, a sharp increase in intracranial pressure is often observed, associated with transient global cerebral ischemia[113], prevented by early external ventricular drainage. The double blood injection model provides good experimental reproducibility to investigate a link between early events, CVS and behavioral deficits. However, when intracranial pressure rapidly increases during the first hours post-SAH[79], it cannot be measured for extended periods in freely moving animals, and treatment by ventricular drainage is not feasible. Moreover, in contrast to patients, the SAH-induced decrease in cerebral blood flow, likely associated with the early onset of microvasospasms, would not depend on intracranial pressure[114,115]. Finally, unlike the SAH patient situation, assessing cell swelling in the acute phase of SAH independently of vasogenic edema remains challenging in small animal models. Therefore, we propose that early cell swelling and cytotoxic edema are directly connected to the cerebral blood flow drop, and ischemic injury rapidly occurs at the time of the initial bleeding, concomitant with secondary edema resulting from blood-brain barrier disruption.

In conclusion, most SAH survivors experience significant neurological sequelae, indicating the need for new therapeutic targets, of which UT is a promising candidate. Based on our study, the biased activity of the UII antagonist urantide toward β-arrestin coupling could be advantageous, but its partial agonistic effect on human UT coupling to Gi/o, Gz, and Gq/PLC/Ca2+/PKC does not support its clinical use[51,116]. The most suitable option for clinical use appears to be GSK1562590, a slowly reversible small molecule hUT antagonist that exhibits an extended duration of receptor occupancy in vivo and complete prevention of UII-mediated effects both in vitro and in vivo. Thus, targeting the UII/UT system to prevent and/or cure the vascular, ischemic, and neurologic consequences of SAH can be considered a new therapeutic intervention targeting early to delayed stages of SAH. Our study also provides a possible therapeutic avenue focusing on UT in other types of diseases involving physiopathology associating perimeningeal cell inflammation such as traumatic brain injury or multiple sclerosis, and leading to long-term cognitive impairment.

Article
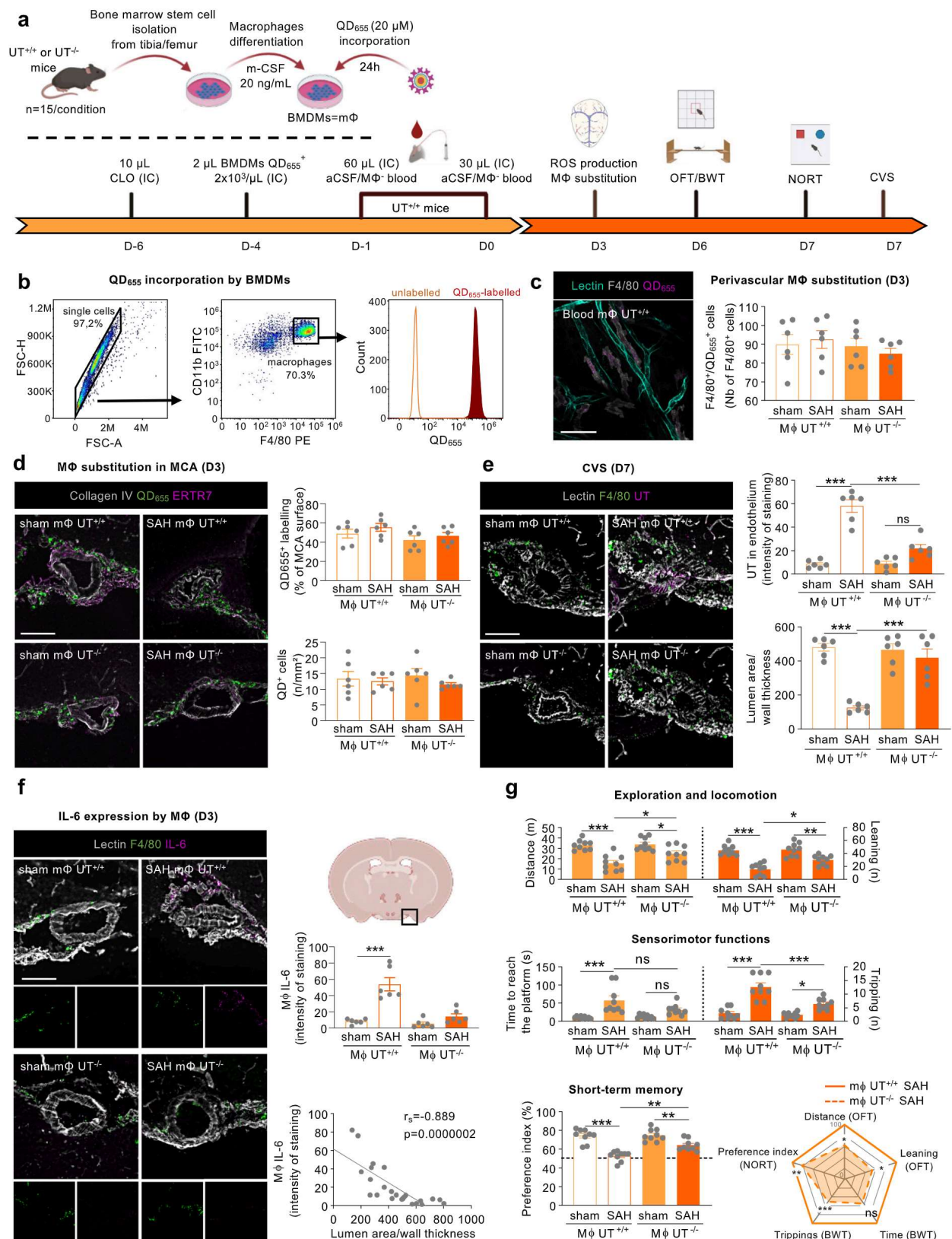
Methods

Animal studies

The experiments were conducted on male C57Bl/6 J Rj mice obtained from Janvier Labs (Le Genest Saint Isle, France) at the age of 7 weeks and divided into different groups. Mice were then in-housed (Animal facility of the University of Rouen Normandie) under controlled standard environmental conditions: $22 \pm 1\,°C$, 8-10 animals per box with enrichment (lignocel®, JRS, Rosenberg, Germany), under a light/dark cycle of 12/12 h, with water and food available *ad libitum*. After an adaptation period, animals were familiarized by regular handling and weighing and cared for via a single-blind procedure. Upon receipt, mice were randomly assigned to surgical and treatment groups. The

Article

Fig. 7 | UT expression in macrophages controls cerebral vasospasm and contributes to behavioral deficits post-SAH. a Timeline of depletion of meningeal and PvMΦs by intracisternal injection of PBS-lip or CLO before intracisternal reinjection of bone marrow isolated MΦs (BMDMs) from UT$^{+/+}$ or UT$^{-/-}$ mice prior to surgery, behavioral testing and CVS analysis. **b** Gating strategy for analysis of incorporation of QD$_{655}$ by F4/80$^+$ CD11b$^+$ BMDMs ($n = 3$). FSC forward scatter, SSC side scatter. **c** Representative QD$_{655}$ (magenta) staining and immunolabeling of F4/80$^+$ MΦs (gray) along lectin$^+$ dural vessels (cyan) of the meningeal dura mater at D3 in UT$^{+/+}$ sham and SAH mice. Quantification of QD$_{655}$/F4/80$^+$ cells among total F4/80$^+$ cells ($n = 6$/condition). Values are expressed as the mean ± SEM. non-significant effect (two-sided two-way analysis of variance (ANOVA), Bonferroni's correction). **d–f** Immunolabeling of Collagen IV$^+$ (green) and nuclei stained by DAPI (white) MCA covered by ERTR7$^+$ leptomeninges (magenta) containing QD$_{655}^+$ cells (red) (**d**) and IL-6 (magenta) and F4/80 (green) along Lectin$^+$ structures (white) at D3 in UT$^{+/+}$ sham and SAH mice intracisternally (IC) injected with UT$^{+/+}$ or UT$^{-/-}$ MΦs labeled with QD$_{655}$ (**d**). Scale bar = 50 μm. (**e**) Immunolabeling of UT (red), F4/80 (green),

and nuclei (white) in MCA at D7 in UT$^{+/+}$ sham and SAH mice injected (IC) with UT$^{+/+}$ or UT$^{-/-}$ MΦs. Quantification of UT intensity in the endothelial and F4/80 MΦ compartments ($n = 6$/condition) and lumen area/wall thickness ($n = 6$/condition). Scale bar = 50 μm. Quantification of QD$_{655}^+$ cells distributed in all conditions (**d**) and of IL-6 staining in F4/80$^+$ MΦ cells (**f**). Spearman test showing a correlation between vasospasm and IL-6 in peri-MCA MΦs ($n = 6$/condition). **g** Exploration in OFT, sensorimotor functions in BWT and preference index in NORT were investigated in sham and SAH mice ($n = 9$/condition). Radar plots illustrating the relative effect of Blood in UT$^{+/+}$ mice injected with UT$^{+/+}$ or UT$^{-/-}$ MΦs on performance in OFT, BWT, and NOR test. Each item of the radar represents the normalized mean. Values are expressed as the mean ± SEM. **c–g** Values are expressed as the mean ± SEM. ns=non-significant, *$P < 0.05$; **$P < 0.01$; ***$P < 0.001$ (two-sided two-way analysis of variance (ANOVA), Bonferroni's correction). Source data are provided as a Source Data file. **a, f** created with BioRender.com released under a Creative Commons Attribution-NonCommercial-NoDerivs 4.0 International license (https://creativecommons.org/licenses/by-nc-nd/4.0/deed.en).

group and sample size for each experiment are indicated in each figure legend. No animal was excluded from the analysis except for some mice that died during or immediately after the SAH microsurgical procedure. This project was approved by the "Comité d'Ethique Normandie en Matière d'Expérimentation Animale", the French Research Minister (APAFIS#17109-201810081437649 v4 and APAFIS#25537-2020052410096594 v2 and APAFIS#25573-2020051410555694 v4) and was performed according to the European Communities Council (Directive 2010/63/EU) guidelines. C57Bl/6 wild-type (UT$^{+/+}$), knock-out (UT$^{-/-}$) and humanized UT (UT$^{h+/h+}$) male mice between 7 and 9 weeks old (20 to 25 g) were used in experiments. We performed the study exclusively in male C57Bl/6 mice due to the reproducibility of the SAH model in males, at least in our hands and according to the recommendations of reducing the number of animals used by the European Directive 2010/63/EU.

For SAH induction and magnetic resonance imaging, animal anesthesia was conducted with inhalant isoflurane (Iso-Vet, Piramal Critical Care, Voorshoten, The Netherlands), 5% for induction and 1.5-2% for maintenance. Analgesia of SAH, sham and donor mice was provided by a subcutaneous injection of buprenorphine (0.1 mg/kg) 30 min before the start of the surgical procedure and if necessary, 6 h after surgery. A protective eye gel (Ocry-gel, TVM Labs, Lempdes, France) was used after the onset of anesthesia to prevent eyes from drying-up during the surgical procedure.

For euthanasia some mice were deeply anesthetized with iso-flurane 5% and then decapitated. Another group of mice (iDISCO) received subcutaneous injection of buprenorphine (0.05 mg/kg, Buprecare, Axience, Pantin, France), then were anesthetized with an intraperitoneal injection of ketamine/xylazine (125 mg/kg, Imalgene 1000, Merial, Lyon, France /12.5 mg/kg, Rompun 2%, Elanco, Sèvres, France) and perfused intracardially with 20 ml of a PBS solution followed by 20 ml of a 4% formaldehyde solution (PFA, prepared from PFA 32%, #15714 S, Electron Microscopy Sciences, Hatfield, USA) and decapitated for brain removal.
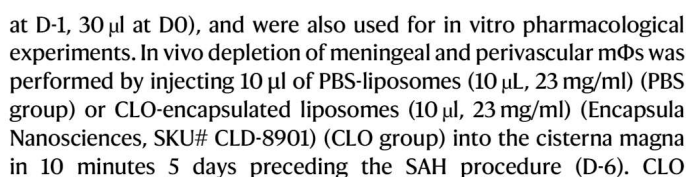
Behavioral assessments
Mice were placed in the experimental room 30 min before the start of each behavioral test. Spontaneous activity and exploration were evaluated by using the open field test (OFT), and sensitivomotor functions were studied by the beam walking test (BWT); anxiety and depressive-like behaviors were investigated by means of the elevated plus maze (EPM) and the forced swim test (FST), respectively. Short-term memory and spatial learning and long-term memory as well as behavioral flexibility were measured with the novel object recognition test (NORT) and Morris water maze test (MWMT). A more detailed description of the behavioral assessment is given in the supplemental methods.

Double intracisternal injection of blood as a model of subarachnoid hemorrhage
The SAH model was established as previously described by injecting two consecutive days of autologous arterial blood into the magna cisterna[27,28] in UT$^{+/+}$, UT$^{-/-}$ or UT$^{h+/h+}$ mice. Briefly, the anesthetized animal was placed in a prone position on a regulated warming blanket in the stereotactic frame with a cervical flexion of approximately 30°. A stretched glass micropipette (GC150F-15, Harvard Apparatus, Edenbridge, UK) filled with the injection solution is advanced using a micromanipulator to cross the atlanto-occipital membrane at a right angle. Two injections (60 μl and 30 μl) were performed with an interval of 24 h. For SAH mice, blood was collected from an autologous mouse anesthetized with iso-flurane at a concentration of 5% in a 50% continuous flow of O$_2$ at 2.5 L/min. For sham mice, an artificial CSF (aCSF) solution was injected. For the first surgery (D-1), skin closure was performed by 2 points of monofil Filapeau type 4.0 (Peters Surgical, Bobigny, France), and a resorbable braided wire Vicryl 4.0 was used for the second surgery (D0). Follow-up of the operated mice included daily weighing and careful behavioral observation. In SAH, in the case of weight loss >15% and/or the presence of pain signs, euthanasia of the animal was performed. A mortality rate of 18.95% was observed exclusively in SAH mice.

Intracisternal administration of pharmacological compounds
Meningeal HIF-1α inhibition was induced by double intracisternal HIF-1α siRNA (ThermoFisher Scientific, #AM16708, ID 158953, 800 pmol/25 μl) or scrambled siRNA (ThermoFisher Scientific, #AM4611, 800 pmol/25 μl) injection for two consecutive days (D-3, D-2) before the SAH procedure. In another experimental set, HIF-1α stabilization was performed by intracisternal injection of the Von Hippel–Lindau (VHL) VH298 inhibitor (10 μl, 5.2 μg/ml) (Tocris, #6156) or aCSF volume as a control 2 h before intracisternal injection of murine UII (50 μl, 2 μg/ml) (Phoenix Pharmaceuticals, #071-08) or aCSF volume solution for two consecutive days (D-1, D0). To evaluate the effect of hemoglobin (Hb) on meningeal hypoxia and UT expression, murine Hb (25 μl, 20 mg/ml) (Cusabio, #CSB-NP004901m) or aCSF solution as a control was intracisternally injected (25 μl) 2 h before UII (2 μg/ml, 50 μl) or aCSF volume solution at D-1 and D0. To control the Gq/PLC and Gi pathways, the Gq inhibitor YM-254890 (0.1 μm) (Adipogen, #AG-CN2-0509), the Gαi/o inhibitor pertussis toxin (PTX, 1 μM) (Sigma Aldrich, #P2980) and the phospholipase C inhibitor (PLC, U73122, 10 μM) (Tocris, #1268) were intracisternally injected in 10 μl of aCSF solution or a CSF volume solution at D-1, 30 min before SAH induction from D-1 to D0. Finally, urantide (synthetized by Dr. Marc André Bonin, peptide synthesis platform, Institut de Pharmacologie de Sherbrooke, Université de Sherbrooke, Quebec, Canada), GSK1562590 (Tocris, #5110) and palosuran (MedChemExpress, #HY-10655) were diluted in blood and intracisternally injected during SAH induction (10^{-5} M, 60 μl

at D-1, 30 µl at D0), and were also used for in vitro pharmacological experiments. In vivo depletion of meningeal and perivascular mΦs was performed by injecting 10 µl of PBS-liposomes (10 µL, 23 mg/ml) (PBS group) or CLO-encapsulated liposomes (10 µl, 23 mg/ml) (Encapsula Nanosciences, SKU# CLD-8901) (CLO group) into the cisterna magna in 10 minutes 5 days preceding the SAH procedure (D-6). CLO

liposomes injected into the subarachnoid spaces should be phagocytized by perivascular mΦs and lead to cell death.

Characterization of cerebral vasospasm on brain slices

After mouse sacrifice by decapitation, collected brains were frozen in isopentane (−30 °C), stored (−80 °C), and then serially sectioned using

Article

Fig. 8 | UT-dependent meningeal plasticity post-SAH controls astrogliosis and some behavioral deficits. a Immunolabeling of ERTR7+ meningeal fibroblasts (magenta) and GFAP+ glia limitans (cyan) in the pia mater and arachnoid from sham and SAH UT+/+ and UT-/- mice at D1. Quantification of meningeal GFAP intensity and area in ERTR7+ areas ($n = 6$/condition). Scale bar = 50 μm. ***$P < 0.001$ (two-way analysis of variance (ANOVA), Bonferroni's correction). **b** Timeline of depletion of meningeal and PvMΦs by intracisternal injection of CLO *versus* PBS-lip in UT+/+ or UT-/- mice, intracisternal reinjection of BMDMs from UT+/+ mice prior to SAH, behavioral testing and CVS/leptomeninges-associated glia limitans reactivity analysis. Immunolabeling of meningeal and perivascular QD655+ (magenta) F4/80+ (white) MΦs along lectin+ brain vessels (green) in SAH UT+/+ mice. Quantification of the percentage of F4/80+/QD655+ cells in meningeal and perivascular areas ($n = 5$). Values are expressed as the mean ± SEM. ns, non-significant effect (normally distributed, comparison of two groups, unpaired two-sided t-test). **c**, **d** Immunolabeling of ERTR7+ meningeal fibroblasts (magenta), GFAP+ glia limitans (cyan) and DAPI (white) in meninges (**c**) or hippocampal fissure (**d**) in sham and SAH UT+/+ and UT-/- mice depleted and reinjected intracisternally with UT+/+ MΦs. Quantification of GFAP areas and intensity in contact with ERTR7+ areas within leptomeninges (**c**) and hippocampal fissure (**d**) ($n = 6$/condition). Scale bar = 100 μm. **e** Quantification of lumen area/wall thickness at D7 ($n = 6$/condition). Scale bar = 50 μm. **f** Exploration in OFT (left panel). Sensorimotor function BWT (right panel) ($n = 10$/condition). Radar plots illustrating the relative effect of blood in UT+/+ and UT-/- mice preinjected (IC) with UT+/+ MΦs on performance in the OFT, BWT, and NOR test. Each item of the radar represents the mean normalized to CLO pretreated Blood UT+/+ mice. (**c-f**) Values are expressed as the mean ± SEM. ns = non-significant, *$P < 0.05$; **$P < 0.01$; ***$P < 0.001$ (two-sided two-way analysis of variance (ANOVA), Bonferroni's correction). Source data are provided as a Source Data file. b created with BioRender.com released under a Creative Commons Attribution-NonCommercial-NoDerivs 4.0 International license (https://creativecommons.org/licenses/by-nc-nd/4.0/deed.en).

a cryomicrotome (#CM 3050S, Leica, Heidelberg, Germany, PRIMA-CEN platform) into 20-μm transverse slices for microscopic fluorescence imaging. Brains were first fixed from the posterior part to the specimen disc with a water-soluble embedding compound (FSC 22®, #3801480, Leica, Heidelberg, Germany). Glass slides were then conserved at −23 °C until use. Nuclear detection by 4′,6-diamidino-2-phenylindole (DAPI, Sigma Aldrich, #D8417) was associated with lectin-FITC conjugate (Vectorlabs, #FL-1171-1) staining for CVS identification characterization. The anterior cerebral (ACA), middle cerebral (MCA) and basilar (BA) arteries were photographed at 40x or 20x magnification using a confocal microscope (Leica SP8 confocal microscope, Leica, PRIMACEN Platform) or a Thunder imaging system (Leica, PRIMACEN). The lumen area and vessel wall thickness were quantified using ImageJ software (Ver.1.45 s, NIH, USA) in a single-blind mode.

Brain water content
Animals were deeply anesthetized with isoflurane 5% and decapitated immediately. After the brains were removed, a 3-mm thick coronal brain slice was cut 4 mm from the frontal pole and divided into two hemispheres along the midline. Afterwards, each hemisphere was dissected into cortex and basal ganglia. The cerebellum served as controls. The samples from each brain were immediately weighed on an electric analytical balance to obtain the wet weight. Then, the brain samples were dried in a gravity oven at 100 °C for 48 h to obtain the dry weight. The brain water content was calculated as follows: (wet weight - dry weight)/wet weight.

Culture of meningeal fibroblasts
For ex vivo culture of meningeal fibroblasts, transparent tissue adherent to the cerebral cortex from the brains of newborn UT+/+, UT-/- or UTh+/h+ mice on postnatal Days 1 to 3 was extracted, and the cerebral meninges were removed piecewise. Then, the pieces were mildly digested with trypsin-EDTA solution (Gibco, #25300054, 0.05%) and filtered through a 70 μm filter (Falcon, #352350). Meningeal cells were attached to poly-L-lysine-coated flasks and cultured in complemented meningeal cell medium (ScienCell, #1401, San Diego, USA) with 10% fetal bovine serum (FBS), 1% penicillin/streptomycin and meningeal cell growth supplement (ScienCell, #1452). In parallel, human meningeal cells (ScienCell, #1400) were cultured in poly-L-lysine-coated flasks in complemented meningeal cell medium (ScienCell, #1401) with 10% FBS, 1% penicillin/streptomycin and meningeal cell growth supplement (ScienCell, #1452).

In vitro calcium assay
Human or murine meningeal cells were plated at 50,000 cells/well into clear-bottom, black, 96-well plates (Corning, #3603, Kennebunk, USA), previously coated with poly-L-lysine and incubated 24 to 72 h in the absence or the presence of VH298 100 μM in culture medium under O_2/CO_2 (5%), and when necessary, pre-incubated for 60 min with Gq, PLCβ or Gi inhibitors: YM-254890 (0.1 μM), U73122 (10 μM), or PTX (1 μM), respectively. Cells were washed twice with modified HBSS (Sigma Aldrich, #P8761) with 10 mM HEPES (Sigma Aldrich, #H0887) and 2.5 mM probenecid, (Sigma Aldrich, #P8761), at pH 7.4 and incubated with Fluo-4AM (Molecular Probes, #F14202, 40 μl, 2 μM) containing pluronic acid (Molecular Probes, #P3000MP), and the effect of graded concentrations of UII on $[Ca^{2+}]_c$ was measured with a FlexStation III (Molecular Devices, Sunnyvale, CA, PRIMACEN). HEK-293 cells transiently transfected with human UT^cmyc were plated at a density of 60 000 cells/well into clear-bottom, black, 96-well plates previously coated with poly-D-lysine (30 μg/mL, 1 h, 37 °C). After 24 h in culture, cells were rinsed twice with HBSS and incubated with Fluo-4AM and pluronic acid. In some experiments, cells were preincubated for 60 min with different ligands (urantide, GSK1562590 or palosuran). The effects of graded concentrations of UII or urantide (10^{-11} to 10^{-6} M, each) on $[Ca^{2+}]_c$ were measured. After subtraction of the mean fluorescence background, the signal baseline was normalized to 100%. Fluorescence peak values were determined for each concentration of UII, and potency (IC_{50}) and efficacy (E_{max}) were calculated with GraphPad Prism-8 software (La Jolla, CA, USA) using a logistic equation. The results are expressed as the mean ± SEM.

Measuring inositol-1 phosphate production
The IP-One assay (Cisbio Bioassays, #62IPAPEB, Bedford, MA) was used to measure inositol 1-phosphate (IP1) levels. Necessary dilutions of each analog were prepared in stimulation buffer (10 mM Hepes, 1 mM CaCl2, 0.5 mM MgCl2, 4.2 mM KCl, 146 mM NaCl, 5.5 mM glucose, 50 mM LiCl, pH 7.4). HEK293-SL were transiently transfected with UT receptor (3 μg) using linear polyethylenimine (Polysciences, #23966; PEI:DNA ratio 3:1). After 48 hours, cells were washed with PBS at room temperature, then trypsinized and distributed at 12,000 cells/well (7 μl) in a white 384-well plate in stimulation buffer. Cells were stimulated at 37 °C for 30 min with increasing concentrations of UII or analogs. For experiments using YM-254890, cells were pretreated for 30 minutes at a final concentration of 100 nM. Cells were then lysed with the lysis buffer containing 3 μL of IP1 coupled to the d2 dye. After addition of 3 μL of anti-IP1 cryptate terbium conjugate, cells were incubated for 3 h at room temperature under agitation. FRET signal was measured using a TECAN M1000 fluorescence plate reader (TECAN, Austria).

BRET-based biosensor assays for Gi, Go, and Gz activation
For Gi, Go and Gz activation assays, HEK293 (10×10^6 cells) were transiently cotransfected with the following constructs: 4 μg SNAP-UT, 2 μg Gα-RLuc8, 2 μg FLAG-β2 and 4 μg Venus-γ2 plasmids in electroporation buffer (50 mM K2HPO4, 20 mM CH3COOK and 20 mM KOH, pH 7.4). Cells were then seeded into black clear bottom 96-well plates
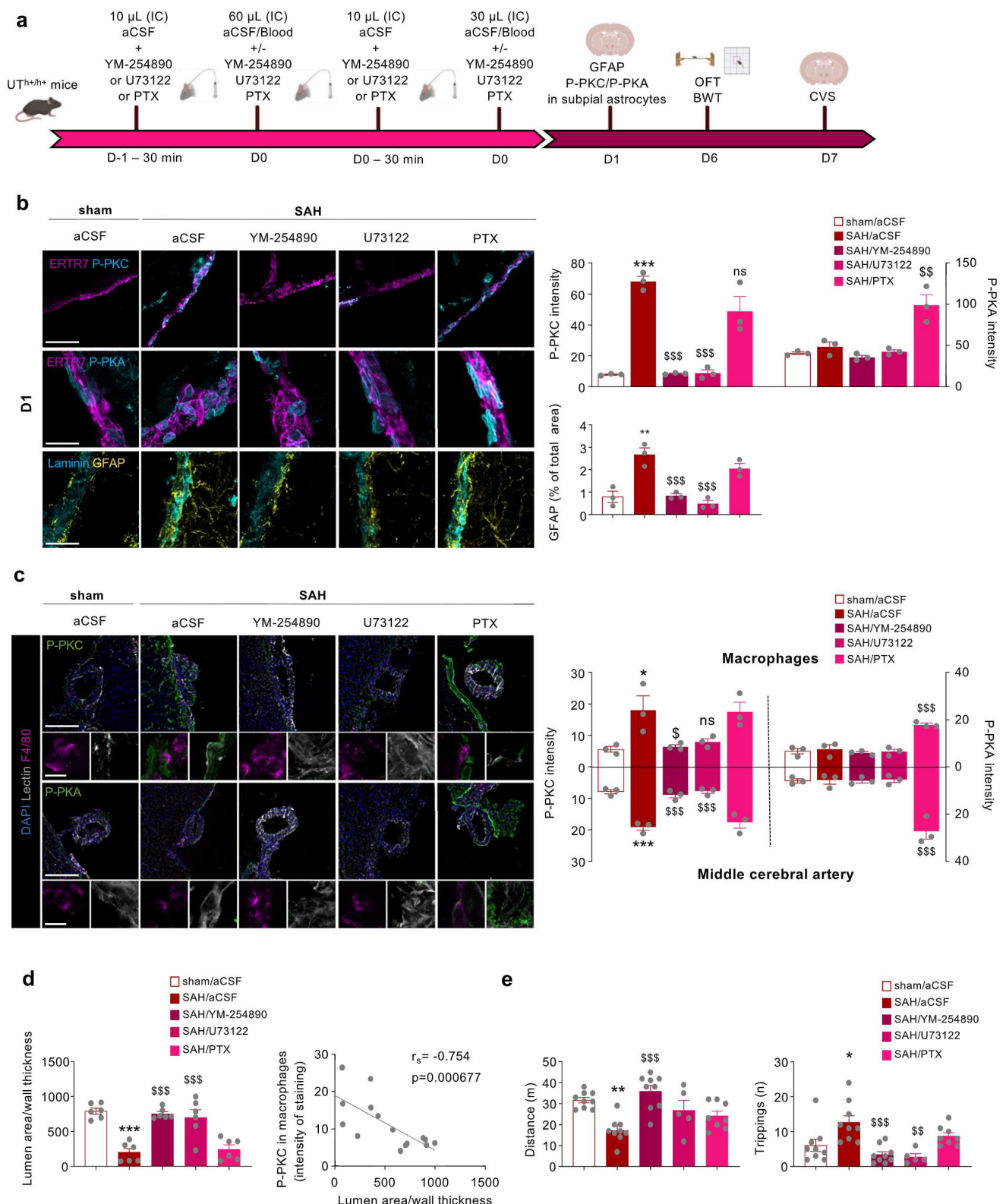
pretreated with poly-L-Ornithine (100 000 cells/well). 24 hours after transfection, cells were washed once with 100 μL PBS1X complemented with 1 mM CaCl2 and 0.5 mM MgCl2. BRET between Rluc8 and Venus was measured after the addition of 40 μL Rluc substrate coelenterazine H (Promega, #S2011, 5 μM). Ligand-promoted BRET was measured after the addition of 40 μL ligands (2X) containing coelenterazine H at 5 μM. BRET readings were collected using a FDSS (Functional Drug Screening System) plate reader (Hamamatsu,

France). The BRET signal was calculated by the ratio of emission of Venus (540 nm) to Rluc8 (480 nm). All data were expressed as a percentage of maximal UII response.

BRET-based biosensor assays for Gq and β-arrestins
For Gq activation assays, HEK293 cells (2×10^6 cells) were transiently cotransfected with the following constructs: 3000 ng of UT, 600 ng Gαq-RLucII, 3000 ng Gγ1-GFP10 and 3000 ng Gβ1, using linear

Fig. 9 | SAH stimulates the UT/Gq/PKC coupling in leptomeninges, dictating delayed cerebral vasospasm and behavioral disorders. a Timeline of intracisternal preinjection of aCSF or YM-254890, U73122, pertussis toxin (PTX), 30 minutes before SAH induction prior to behavioral testing and CVS analysis. **b** Immunolabeling of P-PKC and P-PKA (cyan) in ERTR7⁺ leptomeningeal fibroblasts (magenta) or GFAP (yellow) in contact with ERTR7⁺ fibroblasts was used to measure Gq- and Gi-associated pathway inhibition and astrogliosis at D1 in sham and SHA UT^{h+/h+} mice treated with intracisternal injection of aCSF, YM-254890, U73122 or PTX. Quantification of leptomeningeal P-PKC and P-PKA intensity in the ERTR7⁺ area and GFAP area (n = 3/condition). Scale bar = 20 μm (P-PKA) or 50 μm (P-PKC and GFAP). **c** Immunolabeling of P-PKC and P-PKA (green) in F4/80⁺ MΦs (magenta) around Lectin⁺ (gray) middle cerebral artery (MCA) was used to measure Gq- and Gi- pathway inhibition at D1 in sham and SAH UT^{h+/h+} mice treated with intracisternal injection of aCSF, YM-254890, U73122 or PTX. Quantification of meningeal cells P-PKC and P-PKA intensity in the ERTR7⁺ area (n = 3/condition). Scale bar = 50 μm. Zoomed scale bar = 10 μm. **b, c** Values are expressed as the mean ± SEM. ns, non-significant, $*P < 0.05$; $**P < 0.01$; $***P < 0.001$ for comparisons with the cCSF + sham

condition; $\$\$P > 0.01$; $\$\$\$P < 0.001$ for comparisons with aCSF + SAH condition (two-sided one-way analysis of variance (ANOVA), Tukey's correction). **d** Graphs (right panel) representing changes in lumen area/wall thickness on MCA for CVS measurement (n = 6/condition). Spearman test showing a correlation between vasospasm and P-PKC intensity in peri-MCA MΦs (n = 3/condition). Values are expressed as the mean ± SEM. $*P < 0.05$; $**P < 0.01$; $***P < 0.001$ for comparisons with the cCSF + sham condition; $\$P < 0.05$; $\$\$P > 0.01$; $\$\$\$P < 0.001$ for comparisons with aCSF + SAH condition (two-sided one-way analysis of variance (ANOVA), Tukey's correction). **e** Exploration in OFT and sensorimotor functions in BWT (n = 5–9/condition). Values are expressed as the mean ± SEM. $*P < 0.05$; $**P < 0.01$; $***P < 0.001$ for comparisons with the cCSF + sham condition; $\$\$P < 0.01$; $\$\$$P < 0.001$ for comparisons with aCSF + SAH condition (two-sided one-way analysis of variance (ANOVA), Bonferroni's correction). Source data are provided as a Source Data file. a created with BioRender.com released under a Creative Commons Attribution-NonCommercial-NoDerivs 4.0 International license (https://creativecommons.org/licenses/by-nc-nd/4.0/deed.en).

---

polyethylenimine (PEI:DNA ratio 3:1). For β1-arrestin or β2-arrestin activation assays, HEK293 cells (2 ×10⁶ cells) were transiently cotransfected with the following constructs: 3000 ng of UT, 600 ng of either β1arr-RlucII or β1arr-RlucII and 3000 ng of Caax-rGFP, using linear polyethylenimine (PEI:DNA ratio 3:1). Cells where then seeded into 96-well white plates (20 000 cells/well). After 48 h post-transfection, cells were washed with PBS and resuspended in BRET buffer (10 mM Hepes, 1 mM CaCl2, 0.5 mM MgCl2, 4.2 mM KCl, 146 mM NaCl, 5.5 mM glucose, pH 7.4). For all BRET assays, cells transfected with the appropriate constructs were stimulated with the indicated ligands for 10 minutes. For the antagonism experiments, cells were pretreated with the indicated concentration of UT antagonists before stimulation. Following stimulation, coelenterazine 400 A was added at a final concentration of 5 μM. All BRET signals were measured using a Berthold TriStar2 LB 942 Multimode Reader (Berthold, Bad Wildbad, Germany) with the energy donor filter (410 nm) and energy acceptor filter (515 nm) for GFP10 and rGFP-CAAX. BRET ratio was calculated by dividing acceptor signal over donor signal. All data were expressed as a percentage of maximal UII response.

Preparation and injection of bone marrow monocyte-derived primary macrophages (BMDMs)

Total bone marrow cells were extracted from the tibia and femur of UT^{+/+} or UT^{-/-} mice between 7 and 9 weeks old under a flow of 0.1 M PBS (10 ml), pH 7.4, containing 10% FBS. Cells were centrifuged and resuspended in DMEM (Gibco, #41965039) supplemented with 10% heat-inactivated FBS and 100 ng/ml M-CSF (Miltenyi Biotec, #130-101-706, complete media) at a density of 3×10⁵ cells/ml, seeded onto non-coated 10-cm dishes, and cultured for 5 days in different flasks. On Day 5, cells were treated with free QD_{655} (Molecular Probes, #Q10123MP) in growth medium at 20 nM. The adherent cells are hereafter referred to as bone marrow monocyte-derived primary mΦs (BMDMs)[117]. For injection, cells were centrifuged at 300 × g for 10 min and resuspended in aCSF at 2×10⁶ cells/ml. A volume of 2 μL MΦs derived from UT^{+/+} or UT^{-/-} mice was intracisternally injected into CLO UT^{+/+} or UT^{-/-} mice 2 days after the intracisternal injection of CLO (D-4) and five days before SAH surgery (D-1, D0). In mice pretreated by CLO, blood comes from the donor mouse pretreated with intravenous injection (100 μL) of CLO 24 h before sacrifice to avoid contamination with MΦs of blood during SAH induction.
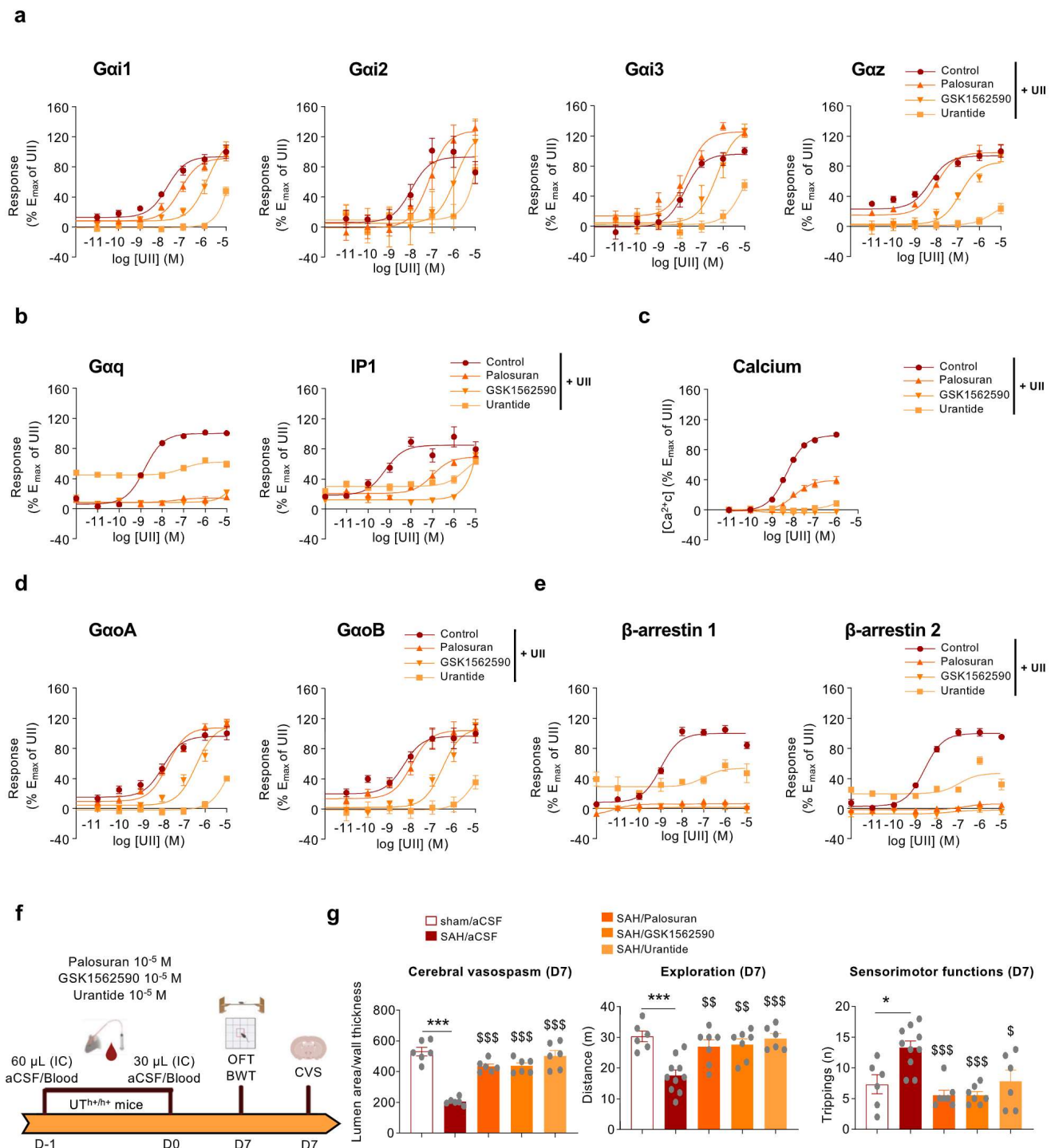
Flow cytometry analysis

Depending on the experiments, BMDMs from UT^{+/+} or UT^{-/-} mice were plated in non-coated plates and incubated with 10 μM VH298 or DMSO (0.1%) as a control for 24 h or with QD_{655} (20 nM) for confirmation of BMDM labeling. Briefly, cells were detached with 0.05% trypsin-EDTA, gently scraped off, and then resuspended in flow cytometry buffer

(PBS without Ca²⁺/Mg²⁺ supplemented with 2% FBS and 2 mM EDTA). Depending on the experimental set, nonspecific binding was blocked by anti-CD16/CD32 (Biolegend, #101302), followed by surface staining with PE-coupled F4/80 (Biolegend, #123110), FITC-coupled CD11b (Biolegend, #101206) or Alexa Fluor 488-conjugated UT (R&D Systems, #FAB9245G), all diluted in flow cytometry buffer. For QD_{655} detection, cells were fixed and permeabilized using the Cytofix/Cytoperm solution kit (BD Biosciences, #554714) according to the manufacturer's protocol. Samples were then acquired on a Cytoflex© (Beckman Coulter, PRIMACEN) equipped with blue and violet lasers followed by data analysis using FlowJo© X software (TreeStar Inc).

Immunohistofluorescence analysis

Brain sections (20 μm) were cut with a cryostat (Leica, #CM1950), post-fixed with 4% PFA (Electron Microscopy Sciences, #15714-s) for 15 min at 4 °C, rinsed in PBS (0.1 M pH 7.4), permeabilized with 0.05% to 0.1% Triton and then incubated overnight at 4 °C with the primary antibody, *i.e.*, sheep anti-BrdU (Abcam, #ab1893) diluted 1:200, mouse anti-NeuN (Abcam, #ab104224) diluted 1:1000, rabbit anti-GFAP (Dako, #ZO334) diluted 1:1000, goat anti-GFAP (Abcam, #ab53554) diluted 1:1000, goat anti-NG2 (Abcam, #ab81104) diluted 1:500, rat anti-podocalyxin (R&D Systems, #MAB1556) diluted 1:500, rabbit anti-αSMA (Abcam, #ab5694) diluted 1:100, rabbit anti-UT (Santa Cruz, #sc-20940) diluted 1:300, goat anti-UT (Santa Cruz Biotechnology, #sc-10194) diluted 1:300, rat anti-CD31 (Abcam, #ab7388) diluted 1:50, rabbit anti-UII (Santa Cruz Biotechnology, #sc-20939) diluted 1:200, rabbit anti-VCAM-1 (Abcam, #ab134047) diluted 1:200, chicken anti-β-galactosidase (Abcam, #ab9361) diluted 1:1000, rat anti-ERTR7 (Abcam, #ab51824) diluted 1:200, mouse anti-AKAP12 (Abcam, #ab49849) diluted 1:100, mouse anti-HIF-1α (Stressgen, #OSA-602) diluted 1:100, rabbit anti-laminin (Sigma Aldrich, #L9393) diluted 1:200, goat anti-F4/80 (Santa Cruz Biotechnology, #sc26642) diluted 1:200, rat anti-F4/80 (Invitrogen, #14-4801-82) diluted 1:200, FITC-conjugated lectin (Vector laboratories, #FL-1171-1) diluted 1:200, rabbit anti-TMEM119 (Abcam, #ab209064) diluted 1:100, rabbit anti-IL-6 (Abcam, #ab208113) diluted 1:200, goat anti-Iba1 (Abcam, #ab5076) diluted 1:100, rabbit anti-fibrinogen gamma chain (Abcam, #ab96532) diluted 1:500, rat anti-Ter-119 (Invitrogen, #14-5921-85), rabbit anti-collagen IV (Novus Biologicals, #NB120-6586), diluted 1:1000, rabbit anti-AKAP12 (Bioss, #bs-138IR) diluted 1:100, rabbit anti-phospho (T497)-PKC (Abcam, #ab59411) diluted 1:200, rabbit anti-PKA alpha/beta/gamma (catalytic subunit) (phospho T197) clone [EP2606Y] (Abcam, #75991) and rabbit anti-active caspase-3 (Abcam, #ab2302) diluted 1:200. Sections were rinsed in PBS and incubated for 2 h at room temperature with appropriate fluorescent secondary antibodies coupled with Alexa Fluor 488 (Invitrogen: donkey anti-sheep, #A11015, donkey anti-goat, #A11055, donkey anti-rat, #A21208;

Abcam: goat anti-chicken, #ab150173), Alexa Fluor 555 (Invitrogen: donkey anti-mouse, #A31570, donkey anti-rabbit, #A31572, donkey anti-goat, #A21432) or Alexa Fluor 647 (Invitrogen: donkey anti-mouse, #A31571, donkey anti-rabbit, #A31573; Abcam: donkey anti-goat, #ab150131, donkey anti-rat, #ab150155) diluted 1:1000 in PBS-Triton 0.25%. Nonspecific binding sites were blocked with normal donkey serum (Sigma Aldrich, #D9663, 10%) from the animal source of the appropriate secondary antibody and control sections were incubated in the absence of primary antibodies. Cell nuclei DNA was stained with DAPI (Sigma Aldrich, #D8417). The stained sections were examined with a confocal microscope (Leica SP8 confocal microscope, Leica, PRIMACEN) or a Thunder imaging system (Thunder Imager Live Cell & 3D Assay, Leica, PRIMACEN).

Meningeal whole mount preparation and immunostaining
Dissection, isolation, and immunostaining of whole meninges were performed as described by Louveau et al.[118]. Briefly, after anesthesia by isoflurane and decapitation, the animal skullcap was harvested in ice-cold PBS containing 5 U/ml heparin (Sigma Aldrich, #H1027) and then placed in 4% PFA for 15 min at 4 °C. After rinsing in PBS, whole meninges were dissected under a microscope by gently scraping the meninges from the skull using fine forceps. For immunostaining, whole mount meninges were incubated on a shaker for 1 h at RT in 300 µl of PBS with 2% normal donkey serum and 1% BSA (Roche, 10735086001), then overnight at 4 °C in primary antibodies, e.g. rat anti-ERTR7 (Abcam, #ab51824) diluted 1:200, FITC-conjugated lectin diluted 1:200, rabbit anti-UT (Santa Cruz Biotechnology, #sc-20940) diluted

Fig. 10 | Cerebral vasospasm and behavioral disorders are efficiently targeted by UT-biased ligand/antagonists. a–e Antagonistic effect of palosuran, GSK1562590 and ligand bias of urantide on the activation of G proteins and β-arrestins in UII-activated UT signaling pathways (3 independent experiments for each in triplicate each). **a** Using BRET[2] biosensors, UII activation of G_i coupled family members Gαi1, Gαi2, Gαi3, and Gαz was assessed in HEK293 cells transiently expressing hUT in the presence of 10 μM of the indicated biased ligand/antagonists. **b** The activation of the G_q pathway was accessed using both a BRET[2] biosensor and by determining the production levels of the second messenger IP_1 in the presence of 10 μM of the indicated biased ligand/antagonists. **c** Ca^{2+} mobilization induced by graded concentrations (10^{-11} to 10^{-6} M) of UII on hUT-transfected HEK-293 cells pretreated with buffer or biased ligand/antagonists. **d** Using BRET[2] biosensors, UII activation of G_o coupled family members GoA and GoB was assessed in HEK293 cells transiently expressing hUT in the presence of 10 μM of the indicated biased ligand/antagonists. **e** Using BRET[2] biosensors, the UII-induced recruitment of β-arrestin 1 and β-arrestin 2 was assessed in HEK293 cells transiently expressing hUT

in the presence of 10 μM of the indicated biased ligand/antagonists (**a–e**, $n = 3$; values are expressed as the mean ± SEM). **f** Timeline of intracisternal injection of palosuran, GSK1562590 or urantide during SAH induction prior to CVS analysis and behavioral testing. **g** Graphs (right panel) representing changes in lumen area/wall thickness on MCA ($n = 6$/condition). Values are expressed as the mean ± SEM. ***$P < 0.001$ for comparisons with aCSF + sham condition. \$\$\$$P < 0.001$ for comparisons with aCSF + SAH condition (two-sided one-way analysis of variance (ANOVA), Bonferroni's correction). Exploration in OFT (10 min) and sensorimotor functions in BWT ($n = 6$–10/condition). Values are expressed as the mean ± SEM *$P < 0.05$; **$P < 0.01$; ***$P < 0.001$ for comparisons with aCSF + sham condition. \$$P < 0.05$; \$\$$P < 0.01$; \$\$\$$P < 0.001$ for comparisons with aCSF + SAH condition (two-sided one-way analysis of variance (ANOVA), Bonferroni's correction). Source data are provided as a Source Data file. **f** created with BioRender.com released under a Creative Commons Attribution-NonCommercial-NoDerivs 4.0 International license (https://creativecommons.org/licenses/by-nc-nd/4.0/deed.en).

1:300 and goat anti-F4/80 (Santa Cruz Biotechnology, #sc-26642) diluted 1:200 in PBS with 1% BSA and 0.5% Triton-X-100. After three rinses in PBS, the meninges were incubated for 1 h at RT in 300 μl of secondary antibodies (Jackson Immunoresearch, donkey anti-rabbit AffiniPure 594, #711-587-003; Abcam, donkey anti-rat Alexa Fluor 647, #ab150155) in PBS with 1% BSA and 0.05% Triton-X-100. Finally, meninges were flattened on a glass slide, dried and mounted in Mowiol (Merck Millipore, #475904) before examination with confocal microcopy imaging.

Brain clearing (iDISCO⁺)
Before clearing, mouse skulls were decalcified by using 0.5 M EDTA once a day for one week. Then, skulls and brain tissues were pretreated according to the protocol of Renier et al.[119]. Briefly, whole brains were dehydrated with exposure to gradual proportions of methanol (Fisher Chemical, #M/4056/17) in PBS (50% X1, 80% X1, and 100% X2, each for 1 h). Overnight bleaching with a 1:5 ratio of hydrogen peroxide (Sigma Aldrich, #H1009):methanol was performed at 4 °C. Tissue was then gradually rehydrated in PBS by removing methanol in 20% increments (1 h for each step, followed by 2 additional washes in PBS). Detergent washing was then performed in PBS with 0.2% Triton X-100 (2X1h). Tissue was incubated overnight at 37 °C in PBS with 0.2% Triton X-100 and 0.3 M glycine (Sigma Aldrich, #G7126), followed by a blocking solution of PBS with 0.2% Triton X-100 and 6% Normal Goat Serum (NGS, Jackson Immunoresearch, 005-000-121) or 0.2% gelatin, depending on primary antibodies. Then, the tissue was washed for 1 h twice in PBS with 0.2% Tween-20 and 10 μg/ml heparin (PTwH). Antibodies were applied at the same concentration as for immunohisto-fluorescence analysis or Osteosense™ (PerkinElmer, #NEV10020EX, 20 nM) for one week in PTwH with 3% NGS at 37 °C with rocking. Excess primary antibodies were washed for 1 day in PTwH with periodic solution changes before starting incubation of secondary antibodies for one week. Then, the tissue was washed in PTwH for 2 days with periodic solution changes. Immunolabeled tissues were cleared by a 3 h incubation of dichloromethane (Sigma Aldrich, #270997):methanol at a 2:1 ratio, 15 min wash (x2) with 100% dichloromethane and 3 h 100% dibenzylether (Sigma Aldrich, #108014). Cleared brains were imaged in sagittal orientation (right lateral side up) with an Ultramicroscope II (LaVision BioTec, Bielefeld, Germany using Imspector-Pro software (LaVision BioTec). The light sheet was generated by a laser at wavelength of 488 nm, 561 nm or 640 nm (Coherent Sapphire Laser, LaVision BioTec). Cleared skulls were imaged in coronal orientation with an Ultramicroscope Blaze (Miltenyi Biotec, Paris, France; PRIMACEN platform). Three-dimensional pictures and tiff series were obtained using the "3D view" and the "animation" tools of the Imaris software. The «filament tracer» tool of the Imaris software was used to determine the diameter and the vascular density of CD31⁺/podocalyxin⁺ labeled vessels in each studied area. Regions of interest

(ROIs) were selected as follows: frontal ($x = 550$ μm, $y = 600$ μm, $z = 300$ μm), parietal ($x = 400$ μm, $y = 400$ μm, $z = 200$ μm), and occipital lobe ($x = 650$ μm, $y = 300$ μm, $z = 200$ μm). Quantitative data are represented as the mean ± SEM.

Magnetic resonance imaging for ventricular volume measurement
MRI was performed at D2 and D6 post-SAH or sham procedure in a 7.0-T Varian MR scanner (Varian Inc) with acquisition of T2* gradient-echo sequences using a field of view of 35×35 mm, matrix of 256×128 mm, and 25 coronal slices (0.5 mm thick). Ventricular volume was measured from the frontal horn of the lateral ventricle to the foramen of Luschka by combining ventricular area over all slices and multiplying by section thickness.

Molecular magnetic resonance for VCAM-1-MPIO imaging
Monoclonal rat anti-mouse CD106 (VCAM-1; Southern Biotech, #1510-01) or mouse IgG1 (Southern Biotech, #0102-01) was conjugated to Dynabeads MyOne Tosylactivated microparticles of iron oxides (MPIOs; Invitrogen, #65501) following the manufacturer's instructions. MPIOs were used at a final concentration of 5 mg MPIO/ml in PBS plus 0.1% BSA and 0.05% Tween 20 at 37 °C. To quantify nanoparticle uptake 2 and 6 days after surgery, 3-dimensional T2*-weighted images were obtained without injection of MPIOs, and 20 min after injection with VCAM-1 MPIO at 1.0 mg Fe/kg body weight.

Functional ultrasound and ultrasound localization microscopy
For imaging sessions, animals were intubated during anesthesia by isoflurane and maintained using an subcutaneous injection of mede-tomidine 0.3 mg/kg (Domitor, Pfizer). Mouse body temperature was kept constant using a heating blanket (Harvard Apparatus, Holliston, MA, USA). The physiological parameters (heart and breathing rates) were followed using MouseOxplus (STARR Life Science, Oakmont, USA). The skull was gently cleaned with saline solution and covered with a centrifuged echographic gel. Acquisitions were performed when the animals had reached a physiological temperature (approximately 45 min after induction) as previously described[40]. Acquisitions were performed on an ultrafast scanner prototype with Neuroscan live acquisition software (ART Inserm U1273 & Iconeus, Paris, France) with a custom ultrasound probe (15 MHz, 0.11 mm pitch, 128 elements). Two positioning scans were performed, in the anteroposterior and sagittal directions, using a 4-axis motor. The coordinate system reference was set on the anteroposterior axis at the vertical plane under the bregma suture $\beta = 0$.

For functional ultrasound imaging, an ultrasound sequence (11 angles from 10° to 10°, increments of 2°) was performed at 500 Hz, and Doppler images were reconstructed at 2.5 Hz (SVD clutter filter cutoff set at 60 singular values). The whiskers were

mechanically stimulated three times for 30 s, interspaced with a 60 s rest period (total duration of the experiment: 300 s). An activation map was reconstructed by computing the normalized correlation between the power Doppler (PD) signal and the stimulation pattern and thresholding above 0.2 (MATLAB, MathWorks Inc., Natick, MA). The relative PD increase was quantified as the mean PD signal in the activated area.

For ultrasound localization microscopy, 100 µl of microbubbles (Sonovue, Bracco, Switzerland) were injected into the tail vein. An ultrasound sequence (-5° 0° 5° transmits) was performed at 1 kHz for 800 ms with a 200 ms pause for a total duration of 180 s. An SVD clutter filter (removal of the first sixty singular values) was used to separate microbubble echoes from tissues. Microbubble centroid positions were first localized and then tracked through consecutive frames using a Hungarian linker (simple tracker). Tracks were interpolated and smoothed using a sliding window of 5 points and cleaned from redundant positions. A density image was reconstructed on an 11 µm × 10 µm grid. The density and flow velocity were quantified using ImageJ software (Ver.1.45 s, NIH, USA) in a blinded fashion. Note that The RBC velocity measurement is highly relevant when vessels are correctly aligned with the probe's imaging plane, as bubbles movement are tracking in this plane. If the bubbles move out of the imaging plane, tracking becomes less precise, if not impossible. For the circle of Willis observed in coronal view for instance, quantifications can be complex as the vessels are more perpendicular to the imaging plane.

Data and statistical analysis

For cell culture, each condition was tested at least in duplicate, and all experiments were repeated at least three times at different passages. Normality was tested using the Shapiro–Wilk test. Multiple comparisons were performed by using unpaired two-sided one-way or two-way ANOVA followed by a Bonferroni's or Tukey's correction. Unpaired two-sided t tests or Mann–Whitney tests (for non-normally distributed data) were used for comparisons of two groups. To test the different evolution day to day (over time) between two groups of mice with sham or SAH condition for instance, and in sham and SAH condition, a Three-way ANOVA was used followed by a Bonferroni's correction. The correlations were calculated by linear regression (Spearman's r_s). Differences were considered significant at $p < 0.05$. Quantification was performed using ImageJ software. Statistical analysis was performed using Sigmaplot software (version 11.0) or Graphpad Prism (version 10.2.2.). Data are presented as the mean ± SEM. Source data are provided with this paper.

Reporting summary

Further information on research design is available in the Nature Portfolio Reporting Summary linked to this article.

Data availability

The data are available within the Article, Supplementary Information or Source Data file. Source data are provided with this paper. The experimental data that support the findings of this study are available in the Supplementary information file. Source data are provided with this paper.

References

1. van der Steen, W. E. et al. Prediction of outcome using quantified blood volume in aneurysmal SAH. *Am. J. Neuroradiol.* **41**, 1015–1021 (2020).
2. Claassen, J. & Park, S. Spontaneous subarachnoid haemorrhage. *Lancet* **400**, 846–862 (2022).
3. Rehman, S. et al. Case-fatality and functional outcome after Subarachnoid Hemorrhage (SAH) in International Stroke Outcomes Study (INSTRUCT). *J. Stroke Cerebrovasc. Dis.* **31**, 106201 (2022).
4. Al-Khindi, T., Macdonald, R. L. & Schweizer, T. A. Cognitive and functional outcome after aneurysmal subarachnoid hemorrhage. *Stroke* **41**, e519–e536 (2010).
5. Nussbaum, E. S., Mikoff, N. & Paranjape, G. S. Cognitive deficits among patients surviving aneurysmal subarachnoid hemorrhage. A contemporary systematic review. *Br. J. Neurosurg.* **35**, 384–401 (2021).
6. Western, E., Nordenmark, T. H., Sorteberg, W., Karic, T. & Sorteberg, A. Fatigue after aneurysmal subarachnoid hemorrhage: clinical characteristics and associated factors in patients with good outcome. *Front. Behav. Neurosci.* https://doi.org/10.3389/fnbeh.2021.633616 (2021).
7. Petruk, K. C. et al. Nimodipine treatment in poor-grade aneurysm patients. Results of a multicenter double-blind placebo-controlled trial. *J. Neurosurg.* **68**, 505–517 (1988).
8. Dorhout Mees, S. M. et al. Calcium antagonists for aneurysmal subarachnoid haemorrhage. *Cochrane Database Syst. Rev.* **2007**, Cd000277 (2007).
9. Francoeur, C. L. & Mayer, S. A. Management of delayed cerebral ischemia after subarachnoid hemorrhage. *Crit. Care* **20**, 277 (2016).
10. Friedrich, V. L. et al. Reduction of neutrophil activity decreases early microvascular injury after subarachnoid haemorrhage. *J. Neuroinflammation* **8**, 103–103 (2011).
11. Provencio, J. et al. CSF neutrophils are implicated in the development of vasospasm in subarachnoid hemorrhage. *Neurocrit Care* **12**, 244–251 (2010).
12. Coulibaly, A. P. et al. Neutrophil enzyme myeloperoxidase modulates neuronal response in a model of subarachnoid hemorrhage by venous injury. *Stroke* **52**, 3374–3384 (2021).
13. Neulen, A. et al. Neutrophils mediate early cerebral cortical hypoperfusion in a murine model of subarachnoid haemorrhage. *Sci. Rep.* **9**, 8460 (2019).
14. Macdonald, R. L. et al. Randomized trial of clazosentan in patients with aneurysmal subarachnoid hemorrhage undergoing endovascular coiling. *Stroke* **43**, 1463–1469 (2012).
15. Naraoka, M. et al. Long-acting statin for aneurysmal subarachnoid hemorrhage: a randomized, double-blind, placebo-controlled trial. *J. Cereb. Blood Flow. Metab.* **38**, 1190–1198 (2018).
16. Takeuchi, S. et al. Intravenous hydrogen therapy with intracisternal magnesium sulfate infusion in severe aneurysmal subarachnoid hemorrhage. *Stroke* **52**, 20–27 (2021).
17. Qureshi, A. I. et al. Therapeutic benefit of cilostazol in patients with aneurysmal subarachnoid hemorrhage: a meta-analysis of randomized and nonrandomized studies. *J. Vasc. Inter. Neurol.* **10**, 33–40 (2018).
18. Wanner, I. B. et al. A new in vitro model of the glial scar inhibits axon growth. *Glia* **56**, 1691–1709 (2008).
19. Bundesen, L. Q., Scheel, T. A., Bregman, B. S. & Kromer, L. F. Ephrin-B2 and EphB2 regulation of astrocyte-meningeal fibroblast interactions in response to spinal cord lesions in adult rats. *J. Neurosci.* **23**, 7789–7800 (2003).
20. Karimy, J. K., Zhang, J., Kurland, D. B., Theriault, B. C. & Duran, D. Inflammation-dependent cerebrospinal fluid hypersecretion by the choroid plexus epithelium in posthemorrhagic hydrocephalus. *Nat. Med.* **23**, 997–1003 (2017).
21. Clavier, T. et al. Association between vasoactive peptide urotensin II in plasma and cerebral vasospasm after aneurysmal subarachnoid hemorrhage: a potential therapeutic target. *J. Neurosurg.* https://doi.org/10.3171/2018.4.jns172313 (2018).
22. Castel, H. et al. The G Protein-coupled receptor UT of the neuropeptide urotensin II displays structural and functional chemokine features. *Front. Endocrinol.* https://doi.org/10.3389/fendo.2017.00076 (2017)

23. Chuquet, J. et al. Effects of urotensin-II on cerebral blood flow and ischemia in anesthetized rats. *Exp. Neurol.* **210**, 577–584 (2008).

24. Cirillo, P. et al. Human urotensin II induces tissue factor and cellular adhesion molecules expression in human coronary endothelial cells: an emerging role for urotensin II in cardiovascular disease. *J. Thromb. Haemost.* **6**, 726–736 (2008).

25. Sun, S.-l & Liu, L.-m Urotensin II: an inflammatory cytokine. *J. Endocrinol.* **240**, R107 (2019).

26. Le Joncour, V. et al. Targeting the urotensin II/UT G protein-coupled receptor to counteract angiogenesis and mesenchymal hypoxia/necrosis in glioblastoma. *Front. Cell Dev. Biol.* https://doi.org/10.3389/fcell.2021.652544 (2021).

27. El Amki, M. et al. Long-lasting cerebral vasospasm, microthrombosis, apoptosis and paravascular alterations associated with neurological deficits in a mouse model of subarachnoid hemorrhage. *Mol. Neurobiol.* **55**, 2763–2779 (2018).

28. Pedard, M., El Amki, M., Lefevre-Scelles, A., Compère, V. & Castel, H. Double direct injection of blood into the cisterna magna as a model of subarachnoid hemorrhage. *J. Vis. Exp.* https://doi.org/10.3791/61322 (2020).

29. Zuo, Y. et al. Neurogenesis changes and the fate of progenitor cells after subarachnoid hemorrhage in rats. *Exp. Neurol.* **311**, 274–284 (2019).

30. Tobin, M. K. et al. Neurogenesis and inflammation after ischemic stroke: what is known and where we go from here. *J. Cereb. Blood Flow Metab.* **34**, 1573–1584 (2014).

31. Burke, M. K., Colin Wilson, F., Curran, D. B. & Dempster, M. A meta-analysis of executive functions among survivors of subarachnoid haemorrhage. *Neuropsychol. Rehabil.* **31**, 1607–1628 (2021).

32. Geraghty, J. R., Lara-Angulo, M. N., Spegar, M., Reeh, J. & Testai, F. D. Severe cognitive impairment in aneurysmal subarachnoid hemorrhage: predictors and relationship to functional outcome. *J. Stroke Cerebrovasc. Dis.* **29**, 105027 (2020).

33. Gallia, G. L. & Tamargo, R. J. Leukocyte-endothelial cell interactions in chronic vasospasm after subarachnoid hemorrhage. *Neurol. Res.* **28**, 750–758 (2006).

34. Martinez de Lizarrondo, S. et al. Tracking the immune response by MRI using biodegradable and ultrasensitive microprobes. *Sci. Adv.* **8**, eabm3596 (2022).

35. Thal, S. C. et al. Brain edema formation and neurological impairment after subarachnoid hemorrhage in rats: Laboratory investigation. *J. Neurosurg.* **111**, 988–994 (2009).

36. Sun, B. L. et al. Effects of blockade of cerebral lymphatic drainage on regional cerebral blood flow and brain edema after subarachnoid hemorrhage. *Clin. Hemorheol. Microcirc.* **34**, 227–232 (2006).

37. Hayman, E. G., Patel, A. P., James, R. F. & Simard, J. M. Heparin and heparin-derivatives in post-subarachnoid hemorrhage brain injury: a multimodal therapy for a multimodal disease. *Molecules* https://doi.org/10.3390/molecules22050724 (2017).

38. Xiao, L., Liu, Y. & Wang, N. New paradigms in inflammatory signaling in vascular endothelial cells. *Am. J. Physiol. Heart Circ. Physiol.* **306**, H317–H325 (2014).

39. Opancina, V., Lukic, S., Jankovic, S., Vojinovic, R. & Mijailovic, M. Risk factors for cerebral vasospasm in patients with aneurysmal subarachnoid hemorrhage. *Open Med.* **15**, 598–604 (2020).

40. Gilbert, A., Elorza-Vidal, X. & Rancillac, A. Megalencephalic leukoencephalopathy with subcortical cysts is a developmental disorder of the gliovascular unit. *eLife* https://doi.org/10.7554/eLife.71379 (2021).

41. Bertolo, A. et al. Whole-brain 3D activation and functional connectivity mapping in mice using transcranial functional ultrasound imaging. *J. Vis. Exp.* **168**, e62267 (2021).

42. Asano, T. & Matsui, T. Antioxidant therapy against cerebral vasospasm following aneurysmal subarachnoid hemorrhage. *Cell. Mol. Neurobiol.* **19**, 31–44 (1999).

43. Pires, P. W. et al. Improvement in middle cerebral artery structure and endothelial function in stroke-prone spontaneously hypertensive rats after macrophage depletion. *Microcirculation* **20**, 650–661 (2013).

44. Faraco, G. et al. Perivascular macrophages mediate the neurovascular and cognitive dysfunction associated with hypertension. *J. Clin. Invest.* **126**, 4674–4689 (2016).

45. Wan, H., Brathwaite, S., Ai, J., Hynynen, K. & Macdonald, R. L. Role of perivascular and meningeal macrophages in outcome following experimental subarachnoid hemorrhage. *J. Cereb. Blood Flow. Metab.* **41**, 1842–1857 (2021).

46. Kuo, L. T. & Huang, A. P. The pathogenesis of hydrocephalus following aneurysmal subarachnoid hemorrhage. *Int. J. Mol. Sci.* https://doi.org/10.3390/ijms22095050 (2021).

47. Okazaki, T. & Kuroda, Y. Aneurysmal subarachnoid hemorrhage: intensive care for improving neurological outcome. *J. Intensiv. Care* **6**, 28 (2018).

48. Macdonald, R. L. et al. Clazosentan, an endothelin receptor antagonist, in patients with aneurysmal subarachnoid haemorrhage undergoing surgical clipping: a randomised, double-blind, placebo-controlled phase 3 trial (CONSCIOUS-2). *Lancet Neurol.* **10**, 618–625 (2011).

49. Kirkpatrick, P. J., Turner, C. L., Smith, C., Hutchinson, P. J. & Murray, G. D. Simvastatin in aneurysmal subarachnoid haemorrhage (STASH): a multicentre randomised phase 3 trial. *Lancet Neurol.* **13**, 666–675 (2014).

50. Gaberel, T. et al. FIVHeMA: intraventricular fibrinolysis versus external ventricular drainage alone in aneurysmal subarachnoid hemorrhage: a randomized controlled trial. *Neurochirurgie* **65**, 14–19 (2019).

51. Brule, C. et al. Biased signaling regulates the pleiotropic effects of the urotensin II receptor to modulate its cellular behaviors. *FASEB J.* **28**, 5148–5162 (2014).

52. Lecointre, C. et al. Signaling switch of the urotensin II vasoactive peptide GPCR: prototypic chemotaxic mechanism in glioma. *Oncogene* **34**, 5080–5094 (2015).

53. Wang, C. et al. Salidroside and isorhamnetin attenuate urotensin II-induced inflammatory response in vivo and in vitro: involvement in regulating the RhoA/ROCK II pathway. *Oncol. Lett.* **21**, 292 (2021).

54. Douglas, S. A., Tayara, L., Ohlstein, E. H., Halawa, N. & Giaid, A. Congestive heart failure and expression of myocardial urotensin II. *Lancet* **359**, 1990–1997 (2002).

55. Maguire, J. J., Kuc, R. E., Wiley, K. E., Kleinz, M. J. & Davenport, A. P. Cellular distribution of immunoreactive urotensin-II in human tissues with evidence of increased expression in atherosclerosis and a greater constrictor response of small compared to large coronary arteries. *Peptides* **25**, 1767–1774 (2004).

56. Loirand, G., Rolli-Derkinderen, M. & Pacaud, P. Urotensin II and atherosclerosis. *Peptides* **29**, 778–782 (2008).

57. Shyu, K.-G., Wang, B.-W., Chen, W.-J., Kuan, P. & Lin, C.-M. Angiotensin II mediates urotensin II expression by hypoxia in cultured cardiac fibroblast. *Eur. J. Clin. Investig.* **42**, 17–26 (2012).

58. Totsune, K. T., Arihara, K., Sone, Z., Ito, M. & Murakami, S. O. Increased plasma urotensin II levels in patients with diabetes mellitus. *Clin. Sci.* **104**, 1–5 (2003).

59. Heller, J. S., Neef, M., Woitas, M., Rabe, R. & Sauerbruch, C. T. Increased urotensin II plasma levels in patients with cirrhosis and portal hypertension. *J. Hepatol.* **37**, 767–772 (2002).

60. Garland, P. et al. Haemoglobin causes neuronal damage in vivo which is preventable by haptoglobin. *Brain Commun.* https://doi.org/10.1093/braincomms/fcz053 (2020).

Article

61. Hugelshofer, M. et al. Haptoglobin administration into the subarachnoid space prevents hemoglobin-induced cerebral vasospasm. *J. Clin. Invest.* **129**, 5219–5235 (2019).

62. Lu, A. Y. et al. Cerebrospinal fluid untargeted metabolomic profiling of aneurysmal subarachnoid hemorrhage: an exploratory study. *Br. J. Neurosurg.* **32**, 637–641 (2018).

63. Akeret, K. et al. Cerebrospinal fluid hemoglobin drives subarachnoid hemorrhage-related secondary brain injury. *J. Cereb. Blood Flow Metab.* **41**, 3000–3015 (2021).

64. Wu, C. et al. Inhibiting HIF-1α by 2ME2 ameliorates early brain injury after experimental subarachnoid hemorrhage in rats. *Biochem. Biophys. Res. Commun.* **437**, 469–474 (2013).

65. Han, J. et al. Distinct volumetric features of cerebrospinal fluid distribution in idiopathic normal-pressure hydrocephalus and Alzheimer's disease. *Fluids Barriers CNS* **19**, 66 (2022).

66. Chen, Y., Galea, I., Macdonald, R. L., Wong, G. K. C. & Zhang, J. H. Rethinking the initial changes in subarachnoid haemorrhage: Focusing on real-time metabolism during early brain injury. *EBioMedicine* **83**, 104223 (2022).

67. Clark, J. F. & Sharp, F. R. Bilirubin Oxidation Products (BOXes) and their role in cerebral vasospasm after subarachnoid hemorrhage. *J. Cereb. Blood Flow Metab.* **26**, 1223–1233 (2006).

68. Segain, J.-P. et al. Urotensin II is a new chemotactic factor for UT receptor-expressing monocytes. *J Immunol* **179**, 901–909 (2007).

69. Ahn, S.-H. et al. Inflammation in delayed ischemia and functional outcomes after subarachnoid hemorrhage. *J. Neuroinflammation* **16**, 213–213 (2019).

70. Zeineddine, H. A. et al. Targeting hemoglobin to reduce delayed cerebral ischemia after subarachnoid hemorrhage. *Transl. Stroke Res.* **13**, 725–735 (2022).

71. Blackburn, S. L. et al. Unique contribution of haptoglobin and haptoglobin genotype in aneurysmal subarachnoid hemorrhage. *Front. Physiol.* **9**, 592–592 (2018).

72. Galea, I. et al. Iron deposition in the brain after aneurysmal subarachnoid hemorrhage. *Stroke* **53**, 1633–1642 (2022).

73. Al Kindi, H. et al. Circulating levels of the vasoactive peptide urotensin II in patients with acute coronary syndrome and stable coronary artery disease. *Peptides* **55**, 151–157 (2014).

74. Vergouwen, M. D., Knaup, V. L., Roelofs, J. J., de Boer, O. J. & Meijers, J. C. Effect of recombinant ADAMTS-13 on microthrombosis and brain injury after experimental subarachnoid hemorrhage. *J. Thromb. Haemost.* **12**, 943–947 (2014).

75. Hutter, B. et al. Functional outcome after aneurysmal subarachnoid hemorrhage. *Acta Neurochir. Suppl.* **72**, 157–174 (1999).

76. Hadjivassiliou, M. et al. Cognitive outcome and structural damage after clipping or coiling. *Neurology* **56**, 1672–1677 (2001).

77. Cai, J. et al. A novel intravital method to evaluate cerebral vasospasm in rat models of subarachnoid hemorrhage: a study with synchrotron radiation angiography. *PLoS ONE* **7**, e33366 (2012).

78. Matsubara, H. et al. Involvement of cerebral blood flow on neurological and behavioral functions after subarachnoid hemorrhage in mice. *J. Stroke Cerebrovasc. Dis.* **30**, 105952 (2021).

79. Dienel, A. et al. Microthrombi correlates with infarction and delayed neurological deficits after subarachnoid hemorrhage in mice. *Stroke* **51**, 2249–2254 (2020).

80. Sun, B. L. et al. Dynamic alterations of cerebral pial microcirculation during experimental subarachnoid hemorrhage. *Cell. Mol. Neurobiol.* **29**, 235–241 (2009).

81. Balbi, M., Koide, M., Schwarzmaier, S. M., Wellman, G. C. & Plesnila, N. Acute changes in neurovascular reactivity after subarachnoid hemorrhage in vivo. *J. Cereb. Blood Flow. Metab.* **37**, 178–187 (2017).

82. Balbi, M., Vega, M. J., Lourbopoulos, A., Terpolilli, N. A. & Plesnila, N. Long-term impairment of neurovascular coupling following experimental subarachnoid hemorrhage. *J. Cereb. Blood Flow. Metab.* **40**, 1193–1202 (2020).

83. Pappas, A. C., Koide, M. & Wellman, G. C. Astrocyte Ca2+ signaling drives inversion of neurovascular coupling after subarachnoid hemorrhage. *J. Neurosci.* **35**, 13375–13384 (2015).

84. Clavier, T. et al. Urantide improves cardiac function, modulates systemic cytokine response and increases survival in a murine model of endotoxic shock. *Shock* **54**, 574–582 (2019).

85. Cha, J. H. et al. Prompt meningeal reconstruction mediated by oxygen-sensitive AKAP12 scaffolding protein after central nervous system injury. *Nat. Commun.* **5**, 4952 (2014).

86. Petry, A. & Görlach, A. Regulation of NADPH oxidases by g protein-coupled receptors. *Antioxid. Redox Signal.* **30**, 74–94 (2019).

87. Lu, D. et al. Urotensin II promotes secretion of LTB(4) through 5-lipoxygenase via the UT-ROS-Akt pathway in RAW264.7 macrophages. *Arch. Med. Sci.* **15**, 1065–1072 (2019).

88. Dong, X. et al. Urotensin II promotes the production of LTC 4 in rat aortic adventitial fibroblasts through NF-κB–5-LO pathway by p38 MAPK and ERK activations. *Heart Vessels* **28**, 514–523 (2013).

89. Watanabe, T. et al. Human urotensin II accelerates foam cell formation in human monocyte-derived macrophages. *Hypertension* **46**, 738–744 (2005).

90. Djordjevic, T. et al. Human urotensin II is a novel activator of NADPH oxidase in human pulmonary artery smooth muscle cells. *Arterioscler Thromb. Vasc. Biol.* **25**, 519–525 (2005).

91. Zheng, V. Z. & Wong, G. K. C. Neuroinflammation responses after subarachnoid hemorrhage: A review. *J. Clin. Neurosci.* **42**, 7–11 (2017).

92. Zhou, C.-H. et al. Urotensin II contributes to the formation of lung adenocarcinoma inflammatory microenvironment through the NF-κB pathway in tumor-bearing nude mice. *Oncol. Lett.* **4**, 1259–1263 (2012).

93. Park, S. L., Lee, B. K., Kim, Y.-A., Lee, B. H. & Jung, Y.-S. Inhibitory effect of an urotensin II receptor antagonist on proinflammatory activation induced by urotensin II in human vascular endothelial cells. *Biomol. Ther.* **21**, 277–283 (2013).

94. Franchini, A. M., Hunt, D., Melendez, J. A. & Drake, J. R. FcγR-driven release of IL-6 by macrophages requires NOX2-dependent production of reactive oxygen species. *J. Biol. Chem.* **288**, 25098–25108 (2013).

95. Ni, W. et al. The relationship between IL-6 in CSF and occurrence of vasospasm after subarachnoid hemorrhage. *Acta Neurochir. Suppl.* **110**, 203–208 (2011).

96. Ridwan, S., Grote, A. & Simon, M. Interleukin 6 in cerebrospinal fluid is a biomarker for delayed cerebral ischemia (DCI) related infarctions after aneurysmal subarachnoid hemorrhage. *Sci. Rep.* **11**, 12 (2021).

97. Croci, D. M. et al. Tocilizumab reduces vasospasms, neuronal cell death, and microclot formation in a rabbit model of subarachnoid hemorrhage. *Transl. Stroke Res.* **12**, 894–904 (2021).

98. Neifert, S. N. et al. Aneurysmal subarachnoid hemorrhage: the last decade. *Transl. Stroke Res.* **12**, 428–446 (2021).

99. Sidharta, P. N., van Giersbergen, P. L. M. & Dingemanse, J. Multiple-dose pharmacokinetics, pharmacodynamics, and safety of the urotensin-II receptor antagonist palosuran in healthy male subjects. *Pharmacology* **102**, 339–346 (2018).

100. Behm, D. J. et al. Palosuran inhibits binding to primate UT receptors in cell membranes but demonstrates differential activity in intact cells and vascular tissues. *Br. J. Pharmacol.* **155**, 374–386 (2008).

101. Clozel, M., Hess, P., Qiu, C., Ding, S. S. & Rey, M. The urotensin-II receptor antagonist palosuran improves pancreatic and renal function in diabetic rats. *J. Pharm. Exp. Ther.* **316**, 1115–1121 (2006).

102. Heidari, S., Babor, T. F., De Castro, P., Tort, S. & Curno, M. Sex and Gender Equity in Research: rationale for the SAGER guidelines and recommended use. *Res. Integr. Peer Rev.* **1**, 2 (2016).

103. Turan, N. et al. Sex differences in the formation of intracranial aneurysms and incidence and outcome of subarachnoid hemorrhage: review of experimental and human studies. *Transl. Stroke Res.* **7**, 12–19 (2016).

104. Harrod, C. G., Batjer, H. H. & Bendok, B. R. Deficiencies in estrogen-mediated regulation of cerebrovascular homeostasis may contribute to an increased risk of cerebral aneurysm pathogenesis and rupture in menopausal and postmenopausal women. *Med. Hypotheses* **66**, 736–756 (2006).

105. Fuentes, A. M., McGuire, L. S. & Amin-Hanjani, S. Sex differences in cerebral aneurysms and subarachnoid hemorrhage. *Stroke* **53**, 624–633 (2022).

106. Duijghuisen, J. J., Greebe, P., Nieuwkamp, D. J., Algra, A. & Rinkel, G. J. Sex-related differences in outcome in patients with aneurysmal subarachnoid hemorrhage. *J. Stroke Cerebrovasc. Dis.* **25**, 2067–2070 (2016).

107. Hamdan, A., Barnes, J. & Mitchell, P. Subarachnoid hemorrhage and the female sex: analysis of risk factors, aneurysm characteristics, and outcomes. *J. Neurosurg.* **121**, 1367–1373 (2014).

108. Lai, P. M. R. et al. Age-dependent radiographic vasospasm and delayed cerebral ischemia in women after aneurysmal subarachnoid hemorrhage. *World Neurosurg.* **130**, e230–e235 (2019).

109. Cai, Y. et al. Comparison of sex differences in outcomes of patients with aneurysmal subarachnoid hemorrhage: a single-center retrospective study. *Front. Neurol.* https://doi.org/10.3389/fneur.2022.853513 (2022).

110. Thompson, J. C. et al. Economic and humanistic burden of cerebral vasospasm and its related complications after aneurysmal subarachnoid hemorrhage: a systematic literature review. *Neurol. Ther.* **11**, 597–620 (2022).

111. Xiong, B. et al. Precise cerebral vascular atlas in stereotaxic coordinates of whole mouse brain. *Front. Neuroanat.* **11**, 128 (2017).

112. Kirst, C. et al. Mapping the fine-scale organization and plasticity of the brain vasculature. *Cell* **180**, 780–795 (2020).

113. van Lieshout, J. H. et al. An introduction to the pathophysiology of aneurysmal subarachnoid hemorrhage. *Neurosurg. Rev.* **41**, 917–930 (2018).

114. Bühler, D., Azghandi, S., Schüller, K. & Plesnila, N. Effect of decompressive craniectomy on outcome following subarachnoid hemorrhage in mice. *Stroke* **46**, 819–826 (2015).

115. Friedrich, B., Muller, F., Feiler, S., Scholler, K. & Plesnila, N. Experimental subarachnoid hemorrhage causes early and long-lasting microarterial constriction and microthrombosis: an in-vivo microscopy study. *J. Cereb. Blood Flow Metab.* **32**, 447–455 (2012).

116. Behm, D. J. et al. The peptidic urotensin-II receptor ligand GSK248451 possesses less intrinsic activity than the low-efficacy partial agonists SB-710411 and urantide in native mammalian tissues and recombinant cell systems. *Br. J. Pharmacol.* **148**, 173–190 (2006).

117. Toda, G., Yamauchi, T., Kadowaki, T. & Ueki, K. Preparation and culture of bone marrow-derived macrophages from mice for functional analysis. *STAR Protoc.* **2**, 100246 (2021).

118. Louveau, A., Filiano, A. J. & Kipnis, J. Meningeal whole mount preparation and characterization of neural cells by flow cytometry. *Curr. Protoc. Immunol.* **121**, e50–e50 (2018).

119. Renier, N. et al. iDISCO: a simple, rapid method to immunolabel large tissue samples for volume imaging. *Cell* **159**, 896–910 (2014).

Author contributions

M.P. performed all surgeries, designed and performed image acquisition studies, performed the main data analysis and wrote the drafted manuscript. M.P., M.D., C.N., L.D., O.W., C.C., and B.H. performed the data analysis. D.G. and O.W. contributed to the 3D iDISCO+ imaging experiments. M.D. and R.G. helped with behavioral studies and their interpretation. M.T. and T.D. developed fUS and ULM acquisition and analysis. M.P., C.A., T.B., D.V., and H.C. conceived the study design and performed FUS and MRI experiments and data analysis. R.L., Lu.P., P.G., and F.M. designed and performed experimental works associated with UT-calcium signaling pathways and UT/PLC/PKC-associated mechanisms. C.C., B.H., La.P., and R.L. designed and performed all experiments on UT coupling to G proteins and β-arrestins by means of BRET/FRET technologies. P.G., F.M., O.W., La.P., R.L., and D.V. provided editorial review and advice. H.C. obtained funding, conceived the idea, experimental design, analysis and interpretation, project supervision, and wrote the drafted and final manuscript.

Competing interests

The authors declare no competing interests.

Additional information

Supplementary information The online version contains supplementary material available at https://doi.org/10.1038/s41467-024-52654-2.

Correspondence and requests for materials should be addressed to Hélène Castel.

Peer review information *Nature Communications* thanks Fumi Nakano, Libin Ye and the other, anonymous, reviewer for their contribution to the peer review of this work. A peer review file is available.

Reprints and permissions information is available at http://www.nature.com/reprints

Publisher's note Springer Nature remains neutral with regard to jurisdictional claims in published maps and institutional affiliations.

Article